



HAL
open science

Structural and petrophysical characterization of mixed conduit/seal fault zones in carbonates: Example from the Castellás fault (SE France)

Christophe Matonti, Juliette Lamarche, Yves Guglielmi, Lionel Marié

► To cite this version:

Christophe Matonti, Juliette Lamarche, Yves Guglielmi, Lionel Marié. Structural and petrophysical characterization of mixed conduit/seal fault zones in carbonates: Example from the Castellás fault (SE France). *Journal of Structural Geology*, 2012, 39, pp.103-121. 10.1016/j.jsg.2012.03.003. hal-02750099

HAL Id: hal-02750099

<https://hal.science/hal-02750099>

Submitted on 25 Nov 2022

HAL is a multi-disciplinary open access archive for the deposit and dissemination of scientific research documents, whether they are published or not. The documents may come from teaching and research institutions in France or abroad, or from public or private research centers.

L'archive ouverte pluridisciplinaire **HAL**, est destinée au dépôt et à la diffusion de documents scientifiques de niveau recherche, publiés ou non, émanant des établissements d'enseignement et de recherche français ou étrangers, des laboratoires publics ou privés.



Distributed under a Creative Commons Attribution - NonCommercial - NoDerivatives 4.0 International License

Structural and petrophysical characterization of mixed conduit/seal fault zones in carbonates: Example from the Castellas fault (SE France)

Christophe Matonti, Juliette Lamarche*, Yves Guglielmi, Lionel Marié

Aix-Marseille University, Geology of Carbonate Systems and Reservoirs Department, Case 67, 3 place Victor Hugo, 13331 Marseille, France

The Castellas fault in SE France affects carbonate rocks with a plurimeter scale offset along 1.5 km of outcrop. In order to decipher the structural control on fault petrophysical and hydraulic character, we performed high resolution field structural mapping, laboratory porosity-Vp measurements, and thin sections analysis of deformations and diagenesis. Field mapping shows that the fault zone architecture displays strong lateral variations at the hectometer scale characterized by core thicknesses of 0–5 m, one or several slip planes, and varying fracture patterns within the damage zone. The fault zone heterogeneity may be related to the magnitude of the throw, the position along the fault and the affected rock facies. Laboratory measurements revealed a strong porosity reduction correlated to a Vp increase, related to the cementation of pore volumes within a decameter area around the fault plane. This fault-sealing occurred mainly through a chemical diagenesis related to fluid circulation within fault-zone heterogeneities. A 3D conceptual model of a mixed conduit/seal fault zone is proposed, characterized by sealed impermeable fault tips and more or less permeable units within which flow can occur either perpendicular or parallel to the fault strike.

1. Introduction

Fault-zone petrophysical characterization is a crucial issue in reservoir exploitation, because fault zones can behave either as hydraulic seal or as conduit. In the first case, fault zones lead to compartmentalizing of the reservoir (Caine et al., 1996); in the second case, they connect porous volumes and drain fluids along high-permeability corridors (Moretti, 1998; Géraud et al., 2006). In addition, combining petrophysical analyses with fault-zone structural characterization is a challenge, because faults may display a number of different hydraulic properties, depending on the presence of an impermeable core, the fault-zone width and complexity, and the diffusivity of the fracture pattern (density, connectivity, and strike).

Faults are discontinuities in rock mass associated with a slip along the fault plane. Strain not only affects the fault plane but also extends into the rock volume, the fault zone. The volume of rock included in a fault zone is commonly divided into three structural parts accommodating increased strain toward the fault plane (Chester and Logan, 1987): (1) the fault core, a centimeter-to-meter-wide area wherein the strain is mainly accommodated,

characterized by fault rocks, and pervasive deformation that obliterates the initial rock facies; (2) the damage zone, a plurimeter-to-hectometer scale wide area containing numerous fractures related to the fault genesis, where fracture density and length decrease with the distance from the fault (e.g. Micarelli et al., 2006b; Blenkinsop, 2008; Mitchell and Faulkner, 2009); (3) the protolith zone, the surrounding undamaged host rock not affected by the fault-related strain. These structural compartments have variable width, depending on fault properties such as the throw, the position along the fault, the rock type and its mechanical properties. In addition, the strain pattern on fault flanks is rarely symmetric (Billi et al., 2003; Micarelli et al., 2006a).

In carbonates, the initial rock-physical properties are highly variable, depending on the depositional facies, and are controlled by biological and sedimentary processes as well as by early diagenesis (e.g. Tiab and Donaldson, 1996; Lucia, 1999). Moreover, carbonates are more sensitive to diagenetic processes than siliclastic rocks (e.g. Anselmetti and Eberli, 1993; Fournier and Borgomano, 2009). Thus, carbonates tend to easily acquire new rock-physical properties (over time and with burial depth) that are quite different from their initial properties. This phenomenon is particularly true along faults, especially where they experience polyphased deformations. Fault-zone properties can drastically change even with respect to shallowly buried (<1 km) and small throw faults. Thus, it is of major importance to couple structural

* Corresponding author.

E-mail addresses: matonti.christophe@free.fr (C. Matonti), Juliette.Lamarche@univ-provence.fr (J. Lamarche).

and deformation approaches with diagenetic and petrophysical measurements, in order to accurately characterize the petrophysical properties within a fault zone and their evolution over time.

More generally, studying field analogs is necessary for hydraulic characterization of faulted reservoirs, in that field analogs enable investigators to reach the less-than-meter resolution that cannot be realized with classical seismic methods. In addition, field investigations allow to characterize the fault zone in three-dimensions and to investigate its property variations along its strike, which is not possible with borehole data. Consequently, this paper is focused on answering the questions: what genetic link exists between rock-physical and architectural properties in a carbonate fault zone? How does a fault zone acquire its petrophysical and hydraulic properties, spatially and over the time? To answer these questions, we characterized and quantified the Castellás fault zone (SE France) architecture and its variations along its strike with meter-scale resolution. We performed a very-high-resolution structural mapping and physical characterization of the fault-zone rock in the region, and finally attempted to determine whether the fault was a potential conduit or seal.

2. Geological settings

2.1. Regional geology

The Castellás fault is located in SE France, in Provence, near Marseille (Fig. 1A). This region is marked by successive tectonic events since early Cretaceous times (Fig. 1B). During early Cretaceous times, southern Provence was affected by an extensional tectonic context favorable for shallow-platform carbonate deposition. During the mid-Cretaceous, a regional uplift (Durance Uplift) led to the emersion and partial erosion of the early Cretaceous carbonates (Masse and Philip, 1975; Guyonnet-Benaize et al., 2010). The late Cretaceous era shows the return to an extensional tectonic and platform conditions in Provence, leading to the deposition of Late Cretaceous carbonates. From the Late Cretaceous, the tectonic context turned to compressional while the basin was located in the foreland of the Pyrénéo-Provençale orogeny. North-verging shortening caused a rise in E–W folds and thrust faults (Fig. 1A). During the Oligocene and Miocene, the tectonic context is extensional, due to West European rifting (Gattacceca, 2001), with a back-arc basin

extension due to the Alpine subduction. From that time, the Alpine orogeny maintained a compressional regime that reactivated earlier Pyrenean folds and thrusts (Leleu, 2005).

2.2. Structural and kinematic context of the fault

The Castellás fault is located on the southern dipping limb of the E–W-striking La Fare ramp anticline. The fold limb is affected by a fault network running mostly parallel to the fold axis, among which is the Castellás fault (Roche, 2008). The fault strikes N060 to N070 (Fig. 2E) and dips 40–80° to the north. Its present-day vertical throw is metric and ranges between 1.5 and more than 5 m (at least) from west to east. We performed a detailed structural analysis of the polyphased kinematics in the field, as well as on samples and thin sections in the laboratory. The kinematic indicators on the fault plane indicate at least two slip episodes (Fig. 2D), the first due to extension, associated with normal dip-slip striations, and the second due to a strike-slip event associated with a strike-slip slickenside (pitch between 2 and 14°E). This latter episode is likely sinistral (Fig. 2E), considering the slickensides. The fault timing was deduced from cross-cutting relationships as well, using calcite veins, stylolites, breccia, open fractures, and overall bed tilting (Fig. 3A–F).

Combining these observations led to the following scenario of fault-zone development. First, the fault formed, affecting the host rock while the bedding was horizontal, which produced a dark breccia (Breccia 1) in the fault core (Fig. 3A) and tension gashes mainly running parallel to the fault plane and present on both sides of the fault plane. The breccia contains angular clasts, laminated and micritic dark matrix, and pendular calcite cements located under and at the clast contacts. These markers suggest that voids opened in the rocks that were subsequently filled by sedimentary matrix during an extensional tectonic context. Second, the host rock is affected by a second breccia (Breccia 2), which cuts through the first breccia (Fig. 3B and C). This breccia is made of smoother clasts surrounded by an orange matrix or by calcite cement. It is affected by numerous randomly distributed stylolites, especially in the first meter closest to the fault plane. Observing the thin sections, we can see that stylolites are emphasized by a dark orange border, likely composed of insoluble clay residues. Rounded breccia clasts are often derived from a thrust or strike-slip fault movement. Thus, these strain markers are associated with

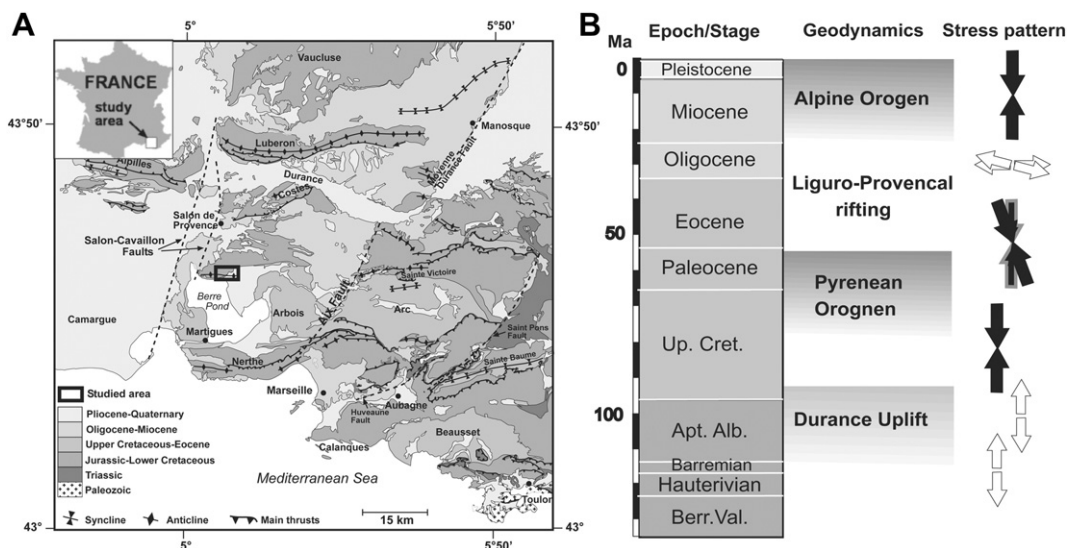


Fig. 1. A. Structural map of south Provence (from Lavenu et al. (in preparation) modified from Lamarche et al. (2010)). B. Tectonic phases and stress regime since Mesozoic (modified from Lamarche et al. (in press)).

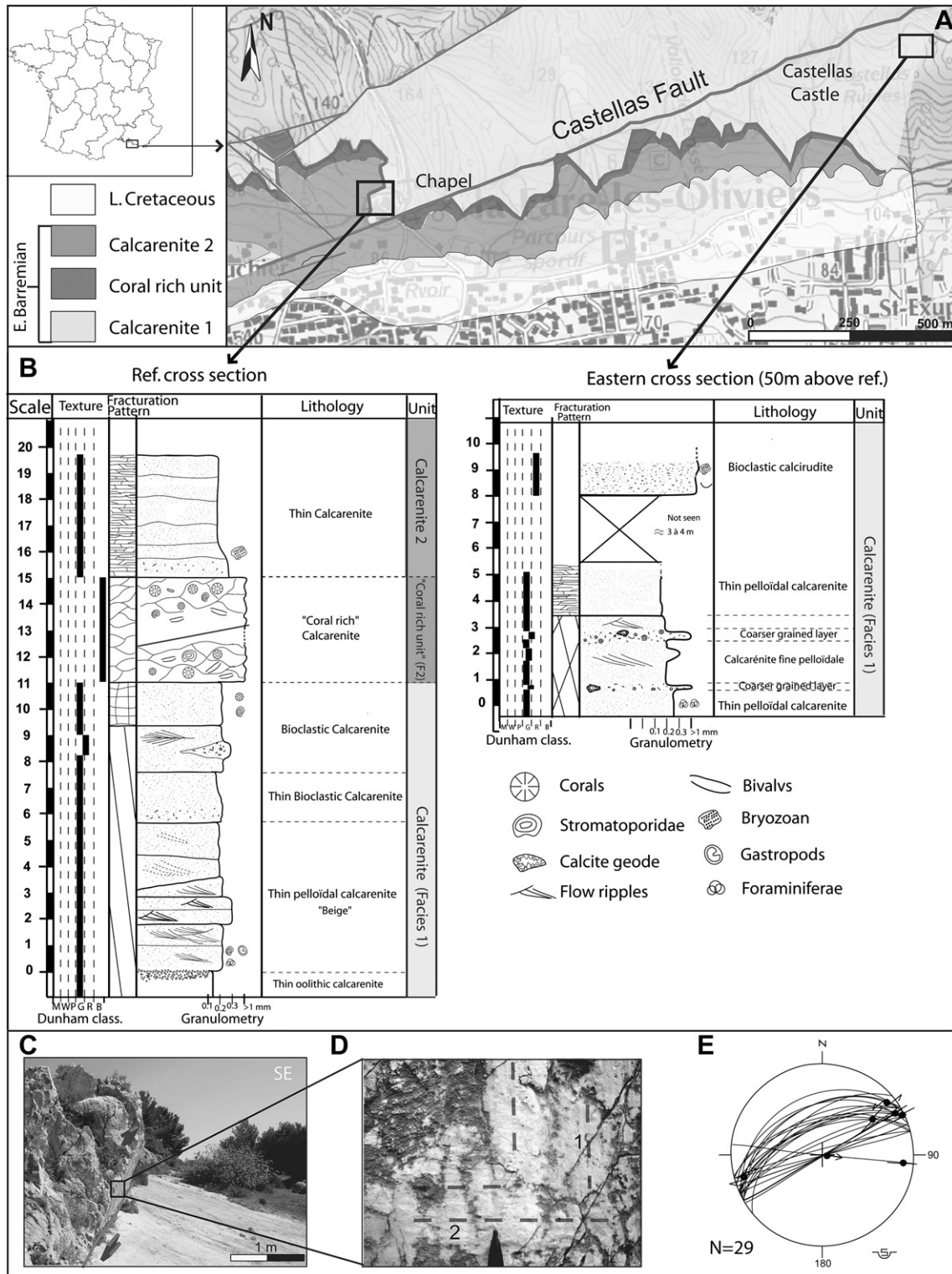


Fig. 2. A. Geological map of the studied area (modified from Roche (2008)). B. Reference sedimentological cross sections. C. Photograph of Castellás fault plane (arrows indicate the blocks relative movements). D. Fault slickensides cross-cutting (1) Strike-slip striae (2) Dip-slip striae. E. Stereoplote of the main fault plane strike and dip (Lower hemisphere projection). Vertical projected plane correspond to plane where only strike was measured.

compressive or transpressive tectonic context. Third, all markers are crosscut by joints that are either opened or partially filled with calcite, located within tens of meters from the fault plane.

This relative timing can be compared to the regional tectonic history. First, Breccia 1 and the tension gashes (1 and 2 in

Fig. 3F) occurred before the overall tilting of the sedimentary layers that took place at the end of the Cretaceous. Therefore, the Castellás fault (and Breccia 1) are likely the result of the Durance Uplift phase, characterized by normal faults during the mid-Cretaceous (Guyonnet-Benaize et al., 2010). Then the

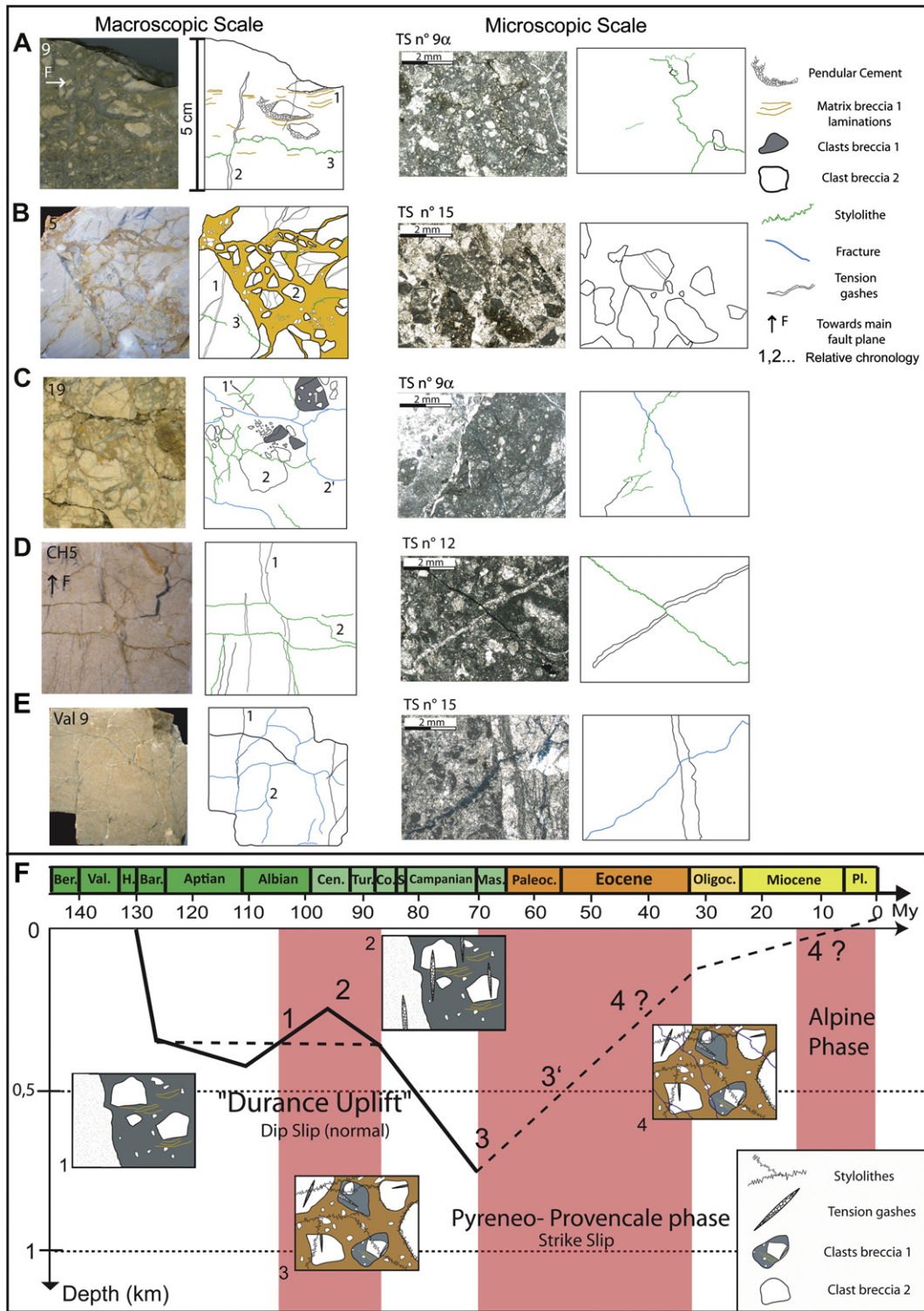


Fig. 3. A–E. Structural analyses on samples (left column) and thin sections (right column), numbers indicate strain marker chronology. F. Relative chronology of strain episodes compared to the burial history and regional tectonic context (burial curve from Jayet (2009)).

sinistral reactivation of the fault occurred, associated with the Breccia 2 and stylolithes (3 and 4 on Fig. 3F). It is associated with the compressive *Pyrenéo-Provençale* tectonic phase that took place from the Maastrichtien to the beginning of the Cenozoïc. Finally, the late joints could be related either to the Pyrenean orogeny or to the alpine orogeny.

2.3. Sedimentary succession of the host rock

The rocks affected by the Castellás fault at the topographic surface belong to the Lower Cretaceous (lower Barremian) carbonate series. They were studied apart from the fault zone, in two outcrops located to the western and eastern boundaries of the

studied area (Fig. 4A). The sedimentary layer succession consists of three units:

1. A basal unit composed of several tens of meters of fine calcarenite with peloidal grains and cross-bedding stratification (Facies 1, Fig. 2B), with a depositional texture of packstone to grainstone (Dunham, 1962). The grains are composed of micritised, benthic foraminifera, and echinoderm bioclasts. This facies is homogeneous along the cross section, but is likely heterogeneous at the hectometer scale because it is part of dune and mega-ripple structures. At the Eastern termination of the study area (Site 5 on Fig. 4A) and over 50 m under the reference cross section, the rock exhibits coarser grains with meter-scale beds of rudstone carbonates.
2. A coral rich carbonate bed composed of fine and very micritised peloidal grains and coarser skeletal elements, with a micritic matrix (Facies 2 on Fig. 2B). A rich fauna is present, with bivalves, corals, and intact stromatoporoidae fossils. This unit is 4–5 m thick and constitutes a marker level visible in the landscape used to infer the vertical throw along the fault.
3. Calcarenite beds composed of fine packstone carbonates, with grains finer than those in Unit 1 (above).

3. Methods

To quantify the structural and petrophysical characteristics of the Castellás fault-zone site and its lateral variability, we conducted our study at three complementary scales, in five different sites along a 1.5 km long outcropping fault zone (Fig. 4A). The study was based on high resolution structural and diagenetic mapping of the fault zone at the meter-to-plurimeter scale, combined with structural analysis of samples coupled to P-wave velocity and porosity

measurements (82 samples) at the centimeter scale, and with thin section analyses to determine the sedimentary and diagenetic facies pore type and microdeformation (50 thin sections) at the micrometer scale.

3.1. Fault-zone structural analyses in the field

Structural mapping was conducted at the meter scale to characterize the fault architecture and its lateral variability. Every 5–10 m across the fault zone, serial cross sections were made perpendicular to the fault strike (transects in Fig. 4B). Along each transect, we mapped the tectonic discontinuities (subsidiary fault or fractures) that individualize structural units. The latter were interpolated across neighboring cross sections in order to reconstruct the fault zone architecture.

Each single structural unit was characterized in terms of fracture pattern (density, length, connections) and the amount of fault induced Cementation and Deformation (CD amount, Figs. 5 and 6). The CD criterion was estimated in the field from the analysis of (1) the fault-related cementation degree (index C) of the host-rock matrix which considers the rock color, the aspect of the rock's broken edge, and the re-crystallization of rock grains (the porosity) and (2) the deformation level (index D) which is determined by the number/quantity of calcite veins, stylolithes, and the presence of breccia and crushed zones (Fig. 5). Four classes were defined from 0 to 3, for C and D respectively (Figs. 5 and 6). A "C" of 0–1 is given to rock samples where the intact rock inter and intragranular porosity is observed (in the field and/or on thin sections). A "C" of 1–2 is given where no porosity is seen and the sedimentary texture is still observed, and a "C" of 2–3 is given to samples where the texture and the porosity are not observable because of recrystallization. A "D" of 0–1 is given to samples where no

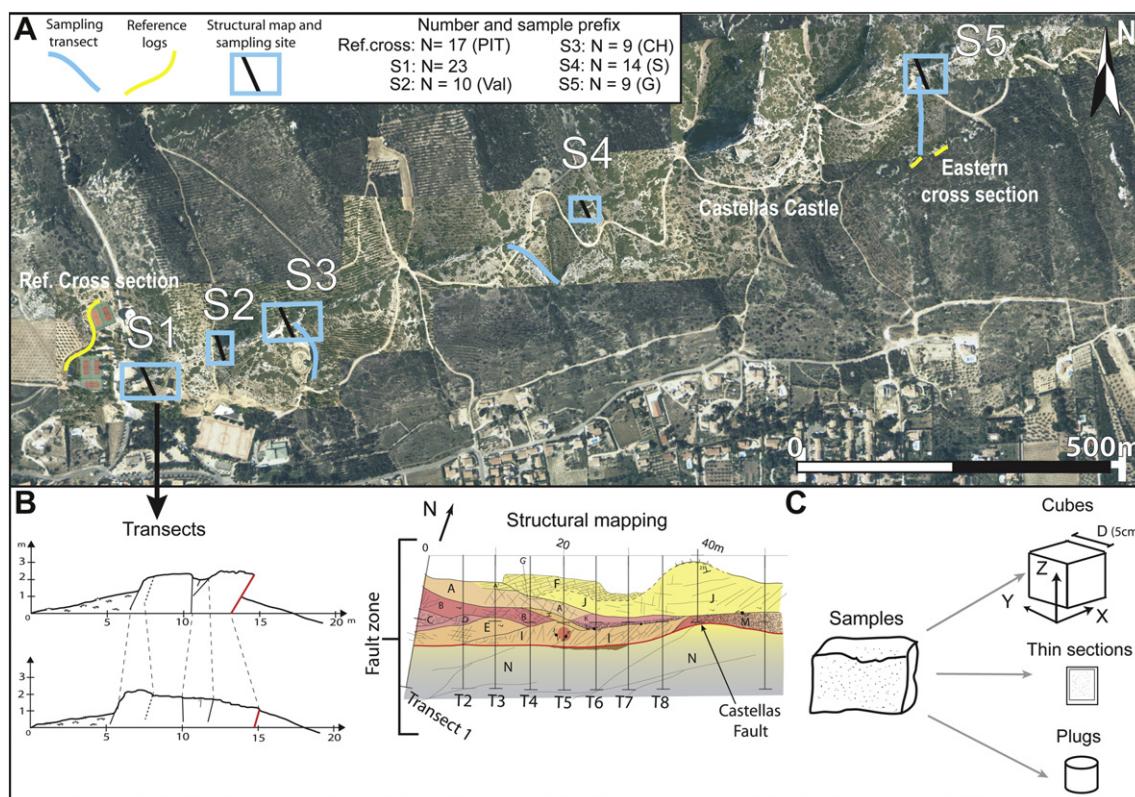


Fig. 4. Method used to perform the study. A. location of the 5 mapped sites along the fault in blue (black lines are the cross section location in Fig. 6) and reference cross sections in yellow. B. High resolution structural mapping method. C. Petrophysical measurements workflow.

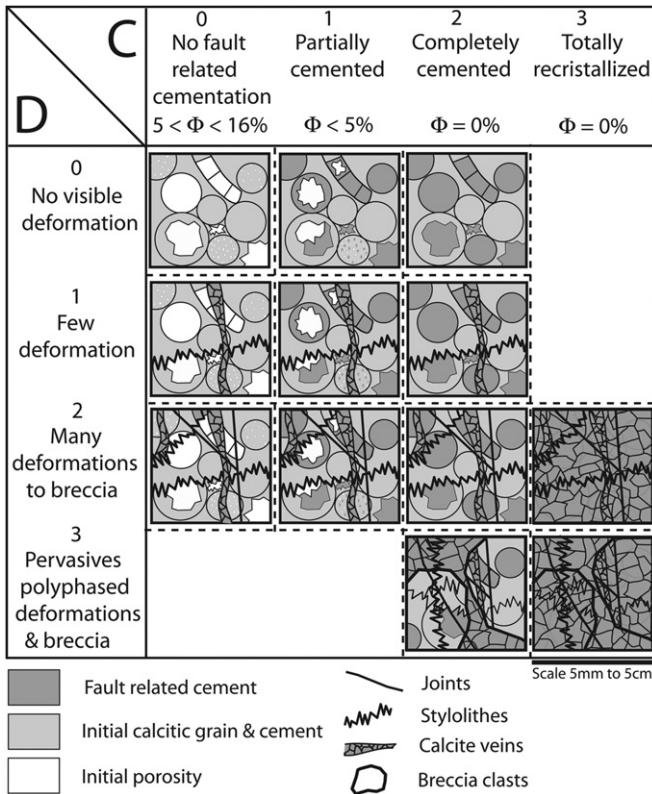


Fig. 5. Cementation (C) and Deformation (D) indexes variations observed on field and samples. CD value is the mean of C and D index (which are not discrete values).

deformation markers are observed. A “D” of 1–2 is given to samples affected by deformations but where the sedimentary and diagenetic textures remain observable. A “D” of 2–3 corresponds to breccia samples. The average of C and D values (CD index) is figured in a color scale from gray to red on maps in Fig. 4 and on cross sections in Fig. 6.

3.2. Rock physics measurements

The P-wave velocities were measured with a Pundit7 apparatus (CNS Farnell Ltd.) on oriented cubic samples (Fig. 4C). Each sample was dried in a stove for 24 h at 60 °C. The portable device measures the travel time of the P-waves between two piezoelectric transducers (emitter/receptor) placed on opposite sides of a sample, with the distance between both transducers determined with an electronic caliper. Therefore, the velocity of the P-wave for the three directions (X, Y, Z), with Z vertical and X toward the fault plane, is determined using the relation $V_p = D/\Delta t$. Before the first measurement, the device is calibrated with a plastic cylinder that has a known travel time. P-wave error was always <5% percent of the measured value. Porosity was measured on 22 cylindrical plugs, each 2.54 cm in diameter and 2.54 cm in length (Fig. 4C). The plugs were drilled into the rock cubes used for the V_p measurements and dried. Their bulk volume was precisely determined by immersion in water. A helium porosimeter was used to measure both macro- (>30 μm) and microporosity (<10 μm). Each measurement was repeated three times to verify the accuracy of the results.

3.3. Microscopic analyses

The host rock and fault-zone porosity were compared on 50 thin sections, with a blue epoxy resin impregnation used on each

section to highlight the porosity. Microstructural analyses were carried out on these thin sections, and evidence of deformation such as tension gashes, clast breccia, stylolites as well as cross-cutting relationship was found. The microscopic diagenetic modifications were compared inside and outside the fault zone for each of the three sedimentary units.

4. Results

4.1. Structural and diagenetic fault structure

The high resolution structural mapping was carried out in five key sites along the fault (Fig. 6). We analyzed the maps in terms of fault-zone width, internal architecture, heterogeneities, fracture patterns, and CD values. All these fault zone attributes present a great variability along the five studied sites which are summarized in Table 1. Moreover, inside a single site, the fault zone show heterogeneities, related to the structural units distinguished in the field (cf. 3.1). In the following section, we comment on five cross sections representatives of each site map. See Appendix 1–5 for a more detailed description of the structural maps, sample location, fault plane stereographic projection and fracture rose diagram.

4.1.1. Fault zone architecture variations

The Castellás fault zone architecture appears complex and highly variable from west to east (Table 1). The fault cuts different sedimentary units, the coral rich bed in the site 1 (facies 2 cf 2.2), the basal unit in sites 2 to 4 (facies 1), and a meter-thick rudstone bed in site 5. The fault zone architecture in the site 1 is composed, in the hanging wall block (North), of a mosaic of 13 anastomosed lenticular structural units bounded by minor faults or decameter fractures (Fig. 6 and Fig. 7A). Two structural units are completely brecciated (unit K site 1 in Fig. 6). In the footwall, no dissimilar structural lenses are distinguishable. In sites 2 and 4, the fault zone architecture is similar, being simpler and more homogeneous than in site 1 (site 2 and 4 in Fig. 6). A discontinuous breccia core occurs in site 2 (unit E in Fig. 6), bounded by decameter fractures delimiting 4 structural units south of the main fault plane. In site 4, the fault zone architecture is even simpler than in site 2, being only composed of one breccia core (unit C site 4 in Fig. 6) surrounded by a damaged zone. The sites 3 and 5, show two main fault planes (Figs. 6 and 7 C and E); delimiting a thick megabreccia core in site 5 and a duplex structure with three sigmoid horses in site 3 sensu Chinnery (1966) (only two are visible in Fig. 6C and called units B and C).

The fault core thickness varies from 0 to 4 m and differs in composition along the Castellás fault (Table 1):

- a few centimeters thick in sites 1, the core is a fault gouge with angular clasts in a very thin micritic dark matrix.
- <1 m thick in site 2, the core is a discontinuous cemented breccia.
- no core sensu stricto in site 3.
- 1–2 m thick in site 4, the core is a continuous poorly cemented breccia.
- at last 4 m thick in site 5, the core is a heterometric megabreccia.

Finally, the strike and dip of the Castellás main fault plane is not constant along the 1.5 km outcrop. Strike ranges from N58 to N075 and dip ranges from 35 to 85°. At the scale of each site (decametric to hectometric), a significant bending of the main fault plane occurs in site 3, characterized by an N059 to N075 variation from west to east.

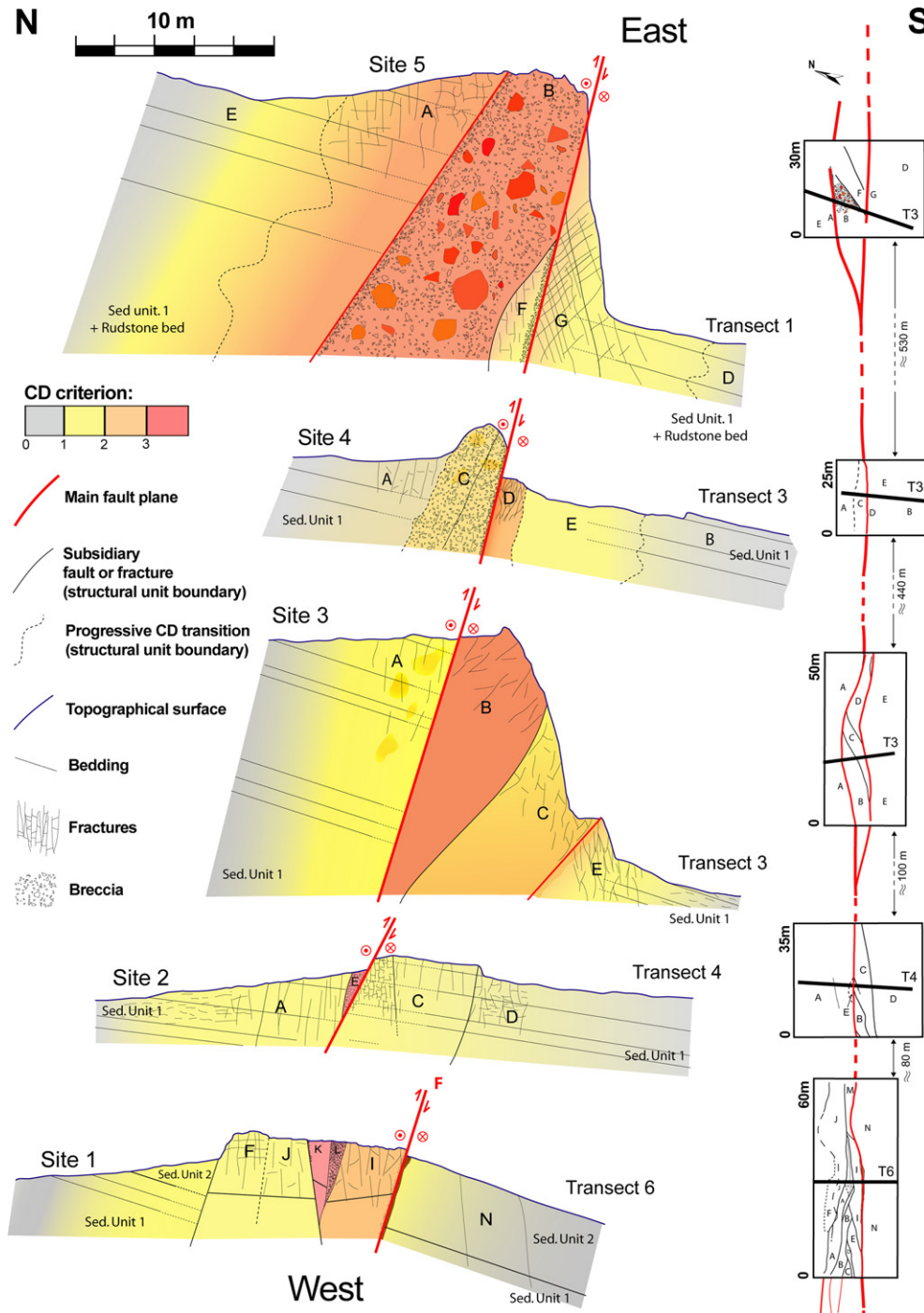


Fig. 6. On the left: Structural cross sections representative of the five studied sites with superimposed CD variations. On the right: Structural maps along the entire Castellás fault (black lines are the transect presented as cross sections).

4.1.2. Fracture pattern types

In the five mapped sites, each structural unit is characterised by different fracture patterns, where the number of sets, strike, length and fracture connectivity vary (Table 1). In sites 1, 3 and 5, the fracture pattern is asymmetric between the footwall and the hanging wall. In site 1, the hanging wall fractures are metric and poorly connected while only a few plurimetric fractures are visible in the footwall (unit N south of the main fault plane). In site 3, the fractures are sub-vertical, dense and highly connected south of the duplex structure (unit E site 3 in Fig. 6) while fewer fractures with

low connectivity occur north of the duplex structure (unit A). The site 5 present the same type of asymmetric fracture pattern. It is dense and connected in the footwall (unit E site 5 in Fig. 6) and sparse and rather unconnected in the hanging wall (unit A). In sites 2 and 4, the fracture pattern is made of highly connected and densely arranged vertical joints. Fractures density increases toward the main fault plane in units A and D of sites 2 and 4, respectively (Fig. 6). Overall, in the five sites, far from the main fault plane (at least 10 m away), the fractures are very sparse or even absent (e.g. unit B in site 4).

Table 1
Architectural and diagenetic attributes of the Castellás fault zone.

	Site 1	Site 2	Site 3	Site 4	Site 5
Brecciated core (width and continuity)	0.1–1 m	<1 m	No fault core sensu. stricto	2 m	4–5 m
Architecture	Discontinuous	Discontinuous		Continuous	Continuous
Complexity	High	Low	High	Low	Average
	Braided/anastomosed lenticular bodies	Homogeneous Decametric fractures	Sigmoidal bodies (duplex structure) between two major fault plane	Structures parallel to the fault	Mega-breccia between two major fault plane
CD mean level	1.93	1.40	1.96	1.24	1.88
Fracturation degree and connexion	Heterogeneous	Intense	Intense in the footwall	Heterogeneous	Intense in the footwall
Facies involved	Poorly connected	Highly connected	Highly connected	Connected	Highly connected
	Facies 2	Facies 1	Facies 1	Facies 1	Facies 1 + Rudstone Bed

4.1.3. CD value variations

The CD criterion represents the level of fault induced rock alteration compared to the unaffected host rock (cf. 3.1). At the whole fault scale, the CD mean values are 1.93–1.40–1.96–1.24–1.88 respectively from sites 1 to 5. The rock remains undeformed ($D = 0$ but $C \neq 0$) at a decameter distance away from the main fault plane, thus the bedding remains clearly visible (Fig. 6). At decameter-scale the CD criterion displays two main types of variations (Fig. 6):

- Highly discontinuous with sharp contrasts in CD values. In site 1, 3 and 5 highly deformed and fault cemented units ($CD = 3$) are intercalated with low deformed and low cemented units ($CD = 1–2$). The site 1 for instance, presents high heterogeneity of the CD value ranging from 0.5 to 3 in a less than 20 m wide space. Moreover, the CD value is not always highest in structural units located closest to the main fault plane. Unit I (sample 7 in Fig. 7A), which is closer to the main fault plane, displays a lower CD than units K and L which are located farther, respectively of 2 m and ~3 m (sample 5 and 7 in Fig. 7A). In site 3, the horse structural units B and C have the highest CD values ($CD > 2$) (Fig. 6). In the unit E, a 50 cm fringe with high CD value bounds the southern fault plane (CH5 in Fig. 7C), then it decreases to 0 a few meters farther to the South (CH3 Fig. 7C).
- Progressive and symmetrical CD variation in both fault compartments in sites 2 and 4. For instance in site 2, CD is low (<1) and homogeneous on the entire fault zone, except in the breccia core (Val 4 in Fig. 7B). In site 4, the highest cemented and deformed zone is not located close to the core that contains a poorly cemented breccia core (unit C, Fig. 6 and S1 in Fig. 7D). Then, CD rapidly decreases to values <0.5 , about 10 m south from the main fault plane (S9 in Fig. 7D).

4.2. Rock physics properties

With the structural and diagenetic fieldwork described above, we were able to accurately choose the best location for samples in the fault zone. A rock-physics characterization based on thin section analyses, Vp, and porosity measurements was carried out on 82 samples from the five studied sites (Table 2). These rock-physics properties were mainly used for comparisons of fault-related diagenesis between the fault zone and the undamaged host rock.

4.2.1. Porosity types and variation

To quantify how the fault zone influences rock porosity, we first determined the amount and type of host-rock porosity outside the fault zone along the reference cross section (Figs. 8–11). The porosity and pore types vary, depending on the rock textural and diagenetic facies being considered. In the calcarenites (Facies 1), the

thin sections show that the porosity is mainly intragranular, forming micro- to mesoporosity located between the micrite crystals. A complete dissolution of the micrite grains led to moldic pores (e.g. TS PIT 07 Fig. 11). Likewise, intergranular porosity resulting from initial partial cementation of intergranular space is rare. In the rudstone layer of facies 1 in the eastern part of the studied area, we observed a high intragranular porosity and numerous moldic pores. In the coral rich facies (Facies 2), most of the porosity is intragranular with a few moldic and vuggy pores. All porosity values measured with a helium porosimeter (Fig. 8) exceed 5% in the undamaged rock. However, a large variability in porosity values was measured within a single facies. For example, samples PIT 07 and PIT 13 from Facies 1 display porosities from 6.6% to 13.4%, and the rudstone porosity is almost 14%. Maximum porosity values of 16.1% have been measured in Facies 2 (S9 sample from site 4).

The porosity values and pore type of the undamaged rock were compared to the fault zone rock. We measured 22 samples in the five sites, in various structural units and at varying distances from the fault (Table 2). Two types of diagenetic transformations were noticed in the damaged rock. First, the rock matrix is affected by several strain markers, depending on the distance to the fault plane and on the mapped structural unit (Figs. 6 and 7). Note that the strain affects grains, cements, and breccia matrix in the same way: no collapsed or deformed grains and no strain markers limited to grain or cement were observed. Secondly, within the fault zone, a systematic porosity decrease is observed toward the main fault plane (Figs. 8 and 9). The pores are filled by microsparitic or macrosparitic calcite cement. Large recrystallized zones are often present, especially in the facies 2, and the initial grains are no longer visible. Inside the fault zone, a few samples showed significant fracture porosity due to late joint opening.

Then we plotted porosity values as a function of distance to the main fault (Fig. 8). The graph points out a clear trend of porosity decrease toward the main fault plane. Rocks in the fault zone have porosity mostly lower than 1%. Outside the fault zone, at a few tens of meters, the average porosity is stable at about 10%.

4.2.2. P-Wave velocity variations

In the undamaged rock of the reference log, the Vp values are similar along X, Y, and Z directions. Indeed the Vx, Vy, and Vz average values for all samples are similar, 5661 m/s, 5887 m/s and 5626 m/s, respectively. However, there are differences in the average Vp, depending on the facies. Facies 1 has a slightly higher velocity (mean Vp = 5346 m/s) than the facies 2 (mean Vp = 5110 m/s).

Vp values in the fault zone were plotted as a function of the main fault distance (Fig. 4A). In site 3, Vp values increase toward the fault (Fig. 9A). From 40 m to 0 m to the fault plane, Vp values clearly increase from 4500 to 6200 m/s. From 60 m to 40 m to the fault plane, the increase is less clear, owing to facies variations (cf. 2.1) and to the bedding dip angle. In site 4, within facies 2, the Vp values

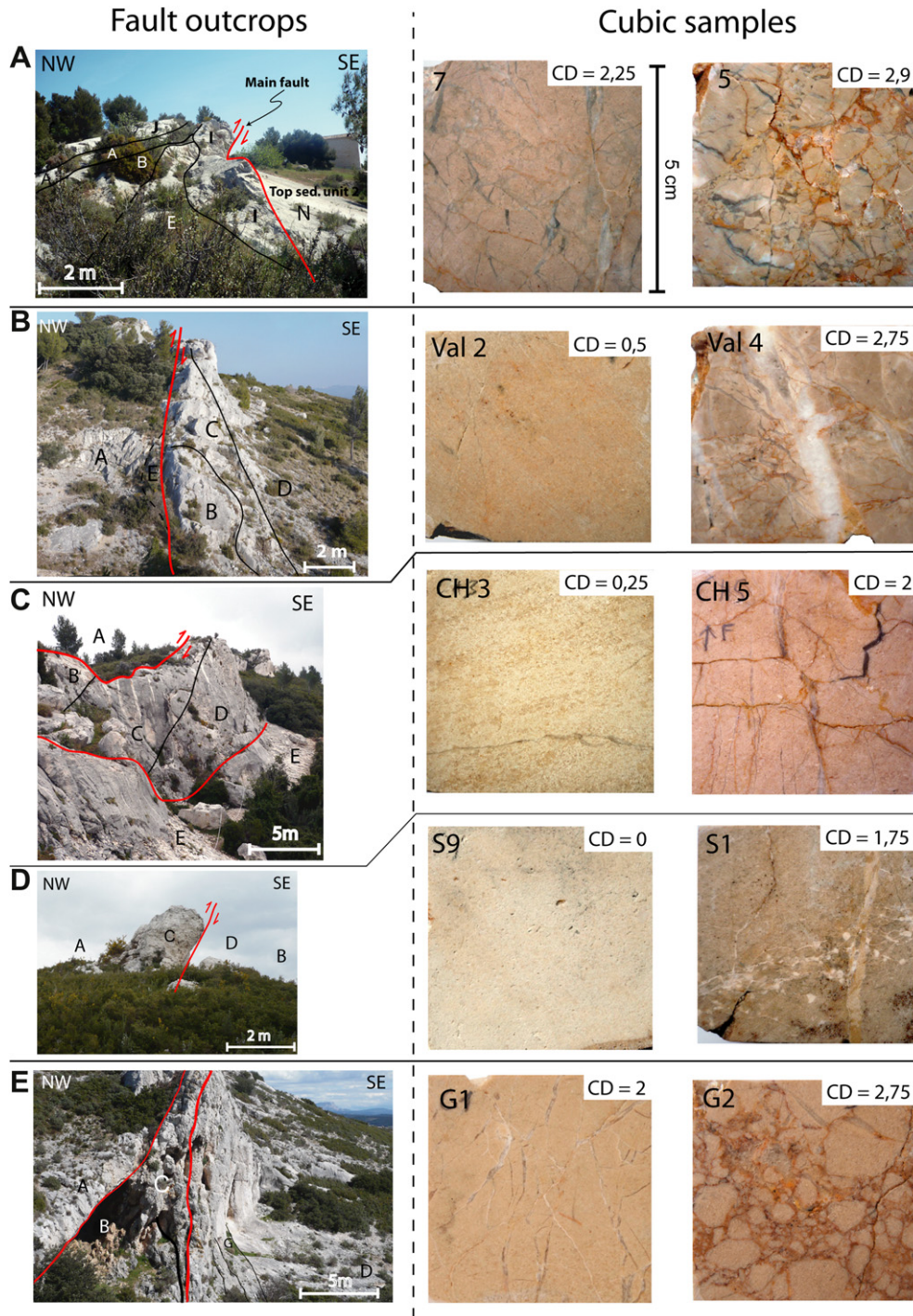


Fig. 7. A–E. On the left, photographs of the fault zone, sites 1 to 5 respectively. On the right, photographs of cubic sample faces from each sites, illustrating different CD values.

sharply increase toward the main fault plane, from 3600 m/s to 6200 m/s between 45 m and 3 m. In site 5, V_p values in the rudstone layer increase toward the fault plane, from 3589 m/s at a distance of 65 m from the fault to 6419 m/s in the fault core (Fig. 9B).

The data show some anomalous values, for example the abnormally low V_z value of 3150 m/s measured for the G4 sample in site 5 is caused by the numerous horizontal open fractures there (photo Fig. 9B). These V_p variations show a clear increasing trend toward the main fault plane. In Fig. 10A shows, this trend exists along the entire fault zone. However, the magnitude of the V_p

increase and the far-field absolute values differ, depending on the site. At site 2 (blue points in Fig. 10A), V_p values are higher (mean $V_p = 6447$ m/s) than at site 4 (mean $V_p = 5019$ m/s, green points, Fig. 10A), even though samples come from the same sedimentary unit (Facies 1).

Overall, the V_p increase reaches 16% over the entire fault zone. Indeed, mean V_p values outside and inside the fault zone are 5321 m/s and 6103 m/s, respectively. Some samples display anomalous low V_p whatever the sector or facies (points circled in red on Fig. 10A). They correspond to samples with numerous open fractures and to samples from breccias.

Table 2
Physical properties and location of 22 samples.

Sample	Site	Facies	Fault distance	Porosity (%)	Vp mean (m/s)	CD value
PIT 13	ref. cross sect.	F1	74	6.6	5248	0
PIT 16	ref. cross sect.	F1	84	5.3	5572	0
PIT 07	ref. cross sect.	F1	78	13.4	5321	0
8	1	F2	0.2	0.4	6306	3
13	1	F2	0	0.6	6716	2.21
16	1	F2	3.7	0.0	6494	2.5
21B	1	F1	20	0.0	6375	0.25
VAL2	2	F1	10	0.5	6643	0.5
VAL7	2	F1	1.6	0.0	6610	0.85
VAL11	2	F1	0.9	0.7	6721	2
CH2	3	F1	60	10.4	4913	0
CH4	3	F1	4	3.4	5968	1
CH5	3	F1	0.5	0.0	6195	2
CH7	3	F1	33	13.2	4556	0
S7	4	F1	2.5	0.2	6194	1.5
S9	4	F1	58	16.1	3604	0
S10	4	F2	45	11.8	3617	0
S12	4	F2	22	8.7	4671	0
G3	5	F1	0	0.2	6419	2
G6	5	F1 (Rudstone)	65	14.0	3589	0
G7	5	F1	140	5.6	5764	0
G10	5	F1	5	0.7	6163	1.5

4.3. Correlation between fault architecture and rock physics

We compared Vp values from all sites to the porosity and the CD variations (Fig. 10B). The Vp values increase is clearly correlated to the CD criterion increase. The average Vp values for each CD classes are 5231 m/s for CD = 0, 5760 m/s for $1 < CD < 2$, 6159 m/s for $2 < CD < 3$, and 6391 m/s for CD = 3. A few low CD samples, mostly located in site 2, have high Vp values. Besides Vp, standard deviations also illustrate the Vp-vs-CD correlation. In site 1, the considerable variability in CD values, related to the high heterogeneity of the fault zone, is associated with the considerable variability in Vp, with a standard deviation of $\sigma = 695$ m/s. At site 2, the relatively homogeneous CD value is associated with low Vp standard deviation ($\sigma = 371$ m/s), in agreement with the homogeneity of the fault zone in this area. P-wave velocities are inversely correlated to the porosity (Fig. 10C). Vp values decrease while the porosity increases

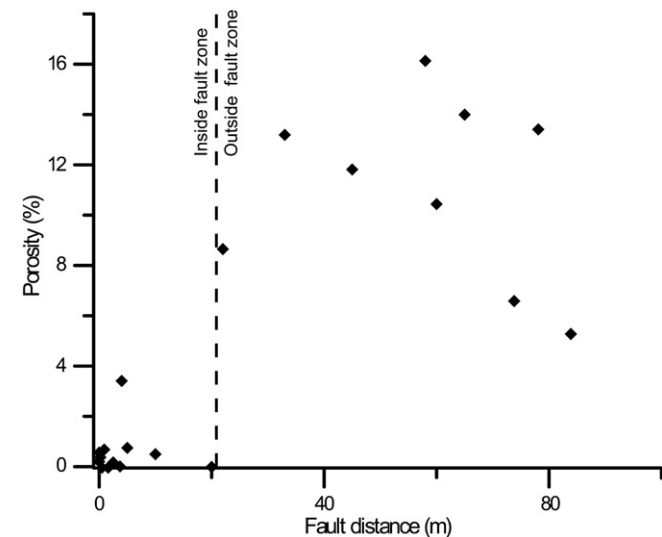


Fig. 8. Rock porosity (%) as a function of the fault distance (m). Dashed line: limit of the fault zone.

($R^2 = 0.86$). Given this good correlation coefficient, it is possible to interpret the Vp value in terms of porosity variation. The correlation between CD, porosity, and Vp, as well as between the standard deviation and the fault-zone complexity, shows the link between fault structure and rock-physics properties.

5. Interpretations and discussions

5.1. Architecture and lateral variations in the fault zone

Structural maps have shown that the Castellás fault zone has a complex and laterally variable architecture, with the variability depending on the specific site or location along the fault (Table 1). For instance, the breccia fault core thickness is less than 1 m and discontinuous at site 2, whereas at site 5, the megabreccia exceeds 5 m in width. The fracture pattern (density and connectivity) is also variable along the fault: intense and highly connected at site 2 and in the footwall of site 3, but rather sparse and poorly connected at site 1. This lateral structural heterogeneity may have different origins (Faulkner et al., 2010). Three hypotheses can be proposed for the Castellás fault:

- (1) **Throw variation:** From west to east, the vertical throw of the main fault increases. At site 1 the apparent vertical throw marked by the coral rich layer (Facies 2) is 1.5 m, but 1 km east, at site 4, the apparent vertical throw exceeds 5 m. Structural studies (Robertson, 1983; Childs et al., 1997; Shipton and Cowie, 2003; Micarelli et al., 2006b; Bastesen and Braathen, 2010) pointed out the correlation between the fault displacement and the core or damage zone width. In the Castellás fault zone, the increasing offset from west to east is in accordance with the observed increased breccia core width.
- (2) **Rock facies variations:** The Castellás fault affects different facies, three of which are visible along the outcrops. Since these facies differ in grain size and in porosity, it could be expected that they display different mechanical (strength) properties (e.g. Sayers, 2008; Baud et al., 2009). Such mechanical contrast could lead to different deformation patterns within both the large-scale fault zone architecture (Steen and Andresen, 1999) and the local fracture pattern (e.g. Di Naccio et al., 2005). For instance, Morris et al. (2009) showed that variable rock-mechanical properties can influence fault nucleation and propagation. Indeed, incompetent layers can inhibit fault propagation. Therefore, the rock facies variation observed in the host rock may be partly responsible for fault-zone heterogeneities.
- (3) **Position along the fault:** According to several studies on fault zone architecture (Peacock, 2002; Kim et al., 2004; Wibberley et al., 2008; Eichhubl et al., 2009), the fault zone internal architecture varies depending on its position along the fault plane. A relay zone often leads to increased complexity and thickening of the fault zone (Childs et al., 1997). A fault tip is characterized by branching structures (Chinnery, 1966; Kim et al., 2004) with synthetic and/or antithetic subsidiary faults. With respect to the Castellás fault, sites 3 and 5 are located on relay stepovers (Twiss and Moores, 1992): they exhibit two main slip surfaces (Figs. 6 and 7). Site 1 is located close to the western fault extremity and shows several branching faults parallel to the main fault plane (Fig. 6 and Table 1). In addition, two subsidiary faults perpendicular to the Castellás fault have been observed to the west of site 1. Finally, sites 2 and 4 may represent simple fault parts, with more offset in site 4 than in site 2. Consequently, the Castellás fault-zone variability may also result from the position of studied sites along the fault trace.

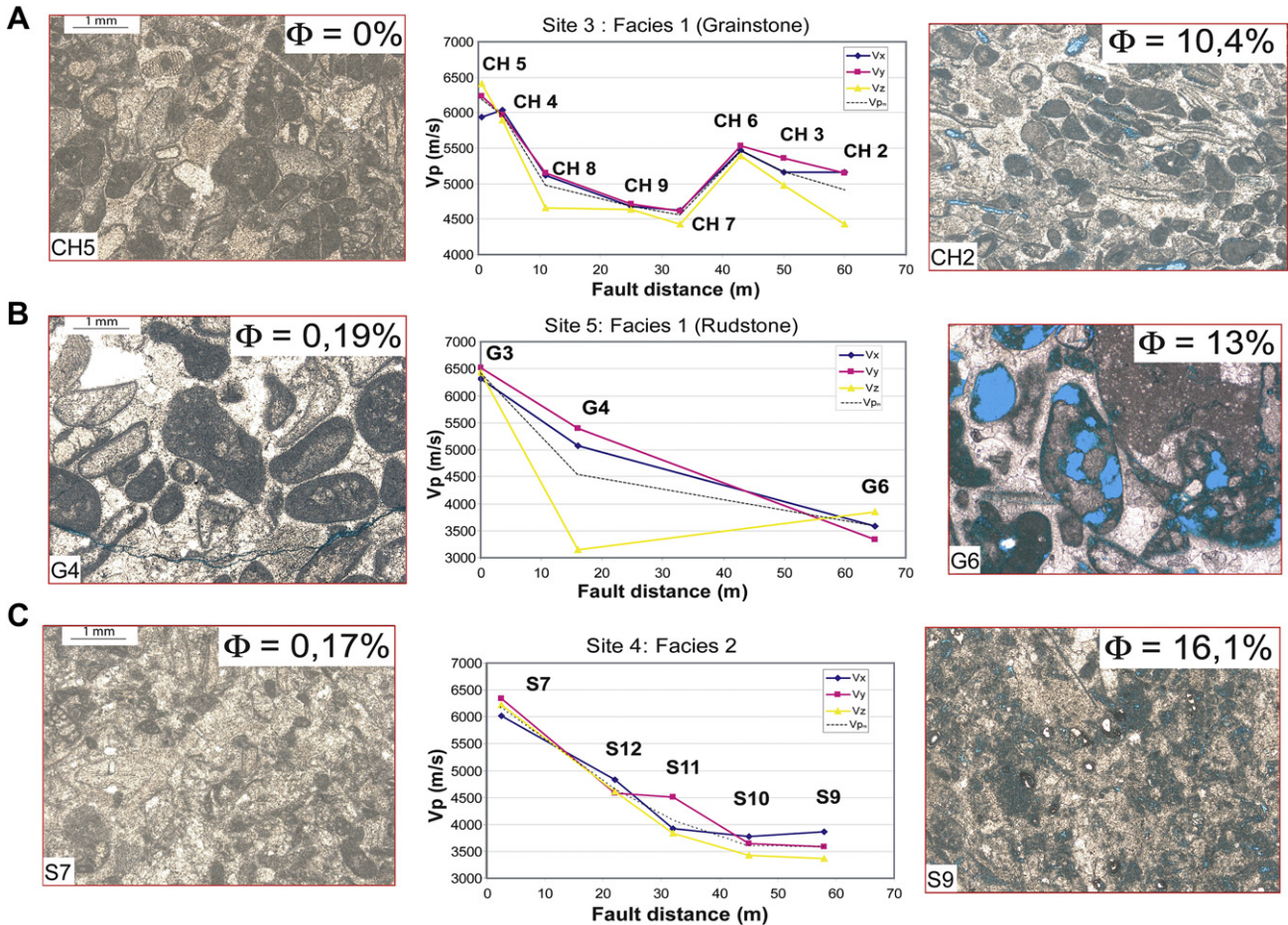


Fig. 9. Vp variations-vs-fault distance on a transect perpendicular to the fault and associated porosity variations inferred from thin sections and plug measurements. A. Facies 1 (grainstone). B. Facies 1 (rudstone). C. Facies 2. Porosity is in blue on thin section photographs.

To conclude, it is difficult to decipher among the three hypotheses presented above. Each one could explain a part of the observed heterogeneity. The influence of intact-rock lithology, for instance, could explain the different fault architectures of sites 3 and 5. Nevertheless, the lithology variation is not strong; the rock remains carbonate on the entire fault outcrop. Thus, increased throw would probably be a more likely explanation for the differences between sites 3 and 5. The position of site 1 close to the fault tip, also where the fault displacement is low, may have more impact on the fault-zone structure than the presence of a coral rich layer (Facies 2). Note that the high resolution structural maps are local windows along the entire fault zone. The maps image only about 200 m of the 1.5 km long Castellás fault. Between the five sites, the fault zone is only partly outcropping. Between sites 3 and 4, the architecture is quite simple: we observed a high fracture density generally located at one side of the fault and a discontinuous cemented breccia core. Between sites 4 and 5, the fault zone is similar to site 4, except at the “Castellás castle” location (Fig. 2), where the fault zone is similar to that observed at site 5. Overall, the Castellás fault zone presents high architecture variability, which seems to be related to multiple factors. It is likely that this structural variability would have an impact on the acquisition and evolution of petrophysical/hydraulic properties along the fault over time.

5.2. Relating Vp and porosity to the fault induced diagenesis

The structural and rock-physics analyses revealed an increase in Vp toward the main fault plane (Figs. 9 and 10). Thin section

analyses and porosity measurements showed a partial-to-total loss of porosity into the fault zone. We observed that the moldic pores and the intragranular microporosity were replaced by sparite cement (Fig. 11). The Vp increase and porosity decrease could thus likely be explained, at least in part, by the cementation of porosity near the main fault plane. Moreover, Eberli et al. (2003) and Fournier et al., 2011 found a strong control of pore types and pore shapes in the sonic velocities within carbonate rocks. Close to the Castellás fault where the rock is not completely cemented, the residual porosity is essentially moldic, partially filled with calcite but also due to open microfractures. These residual pores display different types and shapes compared to the intact rock. As indicated by Eberli et al. (2003) and Fournier et al., 2011, this may be partly responsible for Vp variation within the fault zone. In addition, the replacement of small micrite crystals (<10 μm) by sparite crystals (>50 μm), especially in the totally recrystallised facies 2, is partly responsible for Vp increasing, because micrite and sparite have different mechanical properties (e.g. Vanorio and Mavko, 2011). We notice that the Vp values of ~6 km/s measured in tight rocks of this study are consistent with the usual Vp values measured in highly cemented limestone (e.g. Rafavich et al., 1984).

The precipitation of calcite in pores and micropores close to the fault is possibly a function of CaCO₃-enriched fluids expelled from intense pressure-solution processes. Stylolites are associated with breccia 2 and attributed to the sinistral fault reactivation (see Section 2.2). However, in several studies carried out on carbonate faults (Micarelli et al., 2006a; Tondi et al., 2006; Tondi, 2007; Wibberley and Shimamoto, 2003), the porosity reduction within

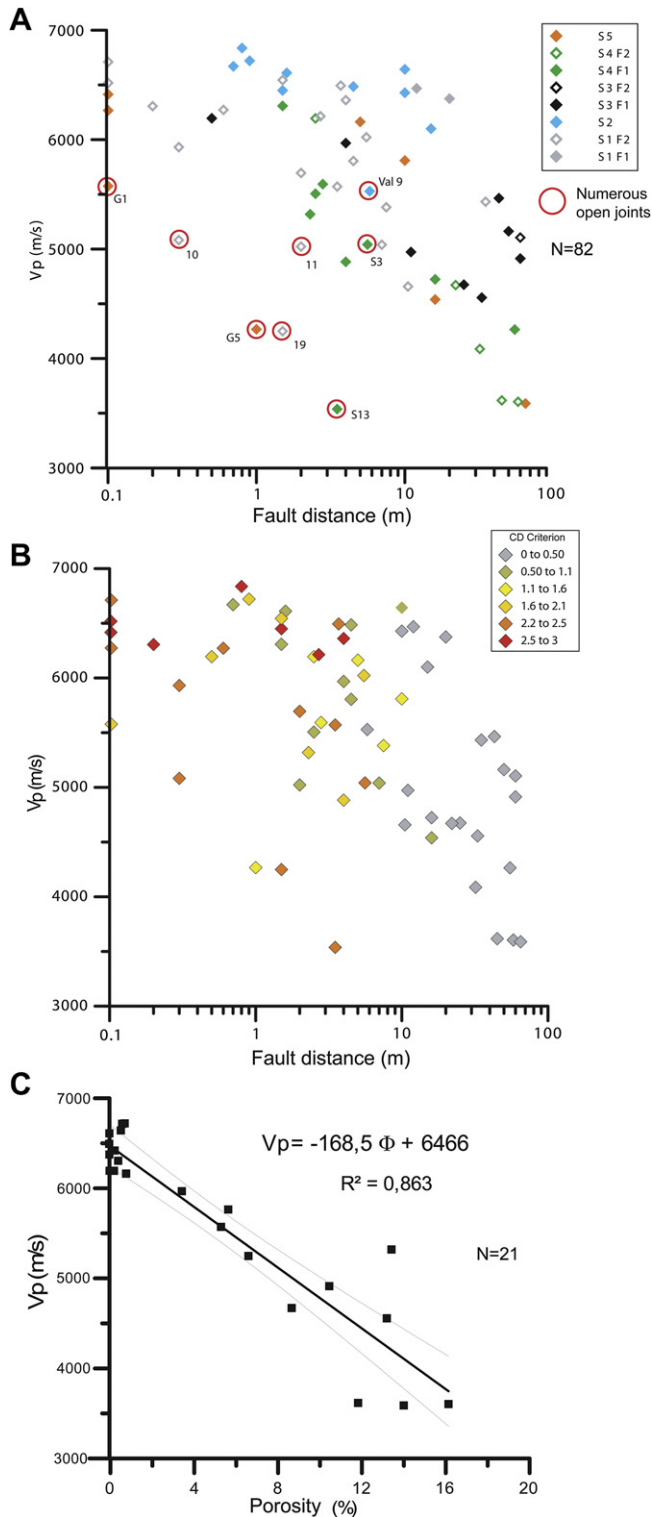


Fig. 10. A. Vp (m/s) variations as a function of fault distance (m), site and facies. B. Vp variations as a function of fault distance and CD criterion classes. C. VP-vs-Porosity (solid line is linear regression).

a fault zone is related to mechanical processes such as grain-size reduction (compaction, abrasion), pore collapse and pressure-resolution. These processes occur in addition to or instead of pore cementation. Grain-scale deformation leading to grain- and pore-preferential orientations (Surma et al., 2003) result in a strong Vp

anisotropy (Martinez-Martinez et al., 2007; Schroeder et al., 2006). However in the present study, no grain-scale deformation such as crushing or grain rotation has been observed. Moreover, the spatial isotropy of Vp values in all samples suggests that the cementation process is isotropic and no stratigraphic or mechanical anisotropy occurs in the rock. Therefore, the porosity reduction close to the Castellás fault is entirely related to cementation by fault induced, CaCO₃-enriched fluids.

5.3. Relating rock-physical properties to the fault zone architecture

Schroeder et al. (2006) and Gaviglio et al., 1999 have also observed an increase in sonic velocities near metric throw faults in carbonate rocks. Their study concerned a decimeter-to-meter fringe around the fault plane. In our study, Vp measurements along transects perpendicular to the main fault plane have shown increases starting at a distance of 30 m from the fault (Fig. 9). Moreover, in the Castellás fault, we found a strong Vp and porosity correlation (cf. Fig. 10C). Thus, in the case of the Castellás fault, the impact of the fault on host-rock physical properties can be significant, reaching several tens of meters in width.

In the Castellás fault, Vp and CD values correlate with one another (Fig. 10A and B), implying that the mesoscale and micro-scale structures are linked within the fault zone. High Vp, and therefore low porosity, correspond to high CD, which are genetically linked to the fault zone architecture. Each structural unit is characterized by a specific CD value. The more structural complexity, the more contrasting CD values (Fig. 6). In addition, the fault zone architecture is related to the thickness of the cemented fringe. In site 1, the fault zone is thick and complex. Vp exceeds 6000 m/s, and the porosity is close to 0% in a zone of >5 m along the main fault plane. Contrarily, in site 4, the fault zone is simpler and thinner; the Vp measured at 3.5 and 4 m from the fault are low (~4000 m/s), suggesting a partially cemented rock. As a consequence, the scattering of Vp values for a given distance to the fault could be explained by the lateral variation in the structural architecture of the fault. The diagenetic alteration is different depending on the fault zone architecture. We have mentioned, however, that Vp variations are also partly a function of the initial rock properties for facies 1 and 2. This is the case in site 2, where samples have high Vp and low porosities, although far from the fault.

To summarize, the Castellás fault impact on rock-physical properties is twofold: (1) it causes a general increase in Vp related to a diagenetic porosity decrease toward the main fault plane, and (2) it causes strong lateral variations closely related to fault zone architecture heterogeneity, which interferes with the diagenetic impact.

5.4. Consequences of fault architecture on hydraulic properties of the fault zone

The structural and rock-physics properties of the Castellás fault can be interpreted in terms of hydraulic properties (Fig. 12). This fault's conduit/seal character can be inferred from our study at two different scales: the micrometer matrix scale and the meter-to-plurimeter fracture scale. Each structural unit can be qualified in terms of specific hydraulic properties.

At the matrix scale, we have shown that the structural units with high CD and high Vp can be considered as tight. Moreover, units with high CD are affected by numerous calcite veins that are impermeable to fluid flow. These structural units are likely to be impermeable seals along the fault. In contrast, structural units with a low CD are more porous and have no or few calcite veins. These units are more permeable to fluid flow and are conduits or normal-permeability flow units along the fault.

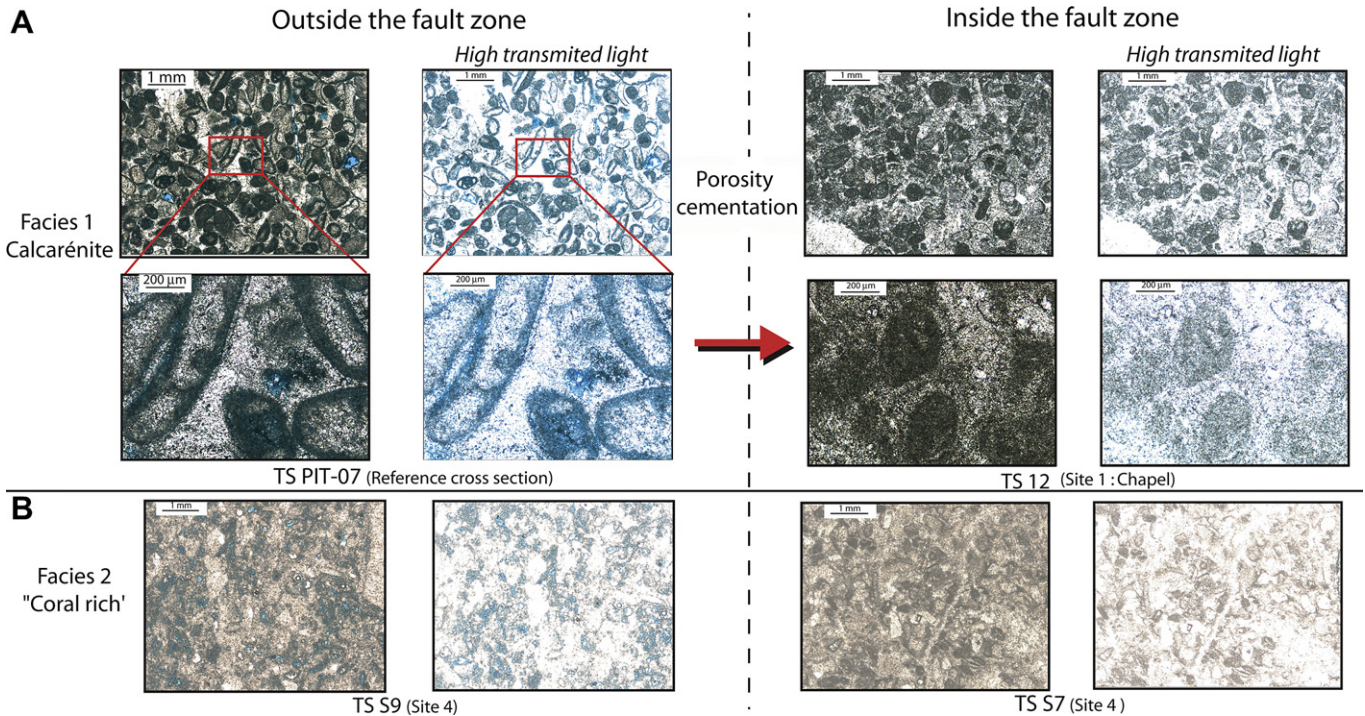


Fig. 11. Porosity cementation on thin sections inside the fault zone. A. Facies 1. B. Facies 2.

At the meter scale, we have to account for fractures. The permeability decrease resulting from diagenetic cementation is balanced by the fracture permeability. Open fractures identified on structural maps represent preferential high-permeability pathways for fluids (Aydin, 2000; Agosta et al., 2010). Fracture connectivity is also crucial for macroscale hydraulic properties of the fault zone (see Marchegiani et al. (2006)). Indeed, unconnected fractures only affect fluid storage but not flow. Considering all these factors, the five sites studied along the Castellás fault zone can be classified into three hydraulic classes:

- (1) *Seal*: site 1 is characterized by numerous structural units, with high CD forming a plurimetric band of cemented rock containing many calcite veins (Figs. 6 and 7A). At the matrix scale, the fault zone at site 1 is a seal to fluid flow. At the metric scale, fracture density is low and insufficiently connected to enhance the drain effect. Consequently, in buried subsurface conditions, site 1 would be a hydraulic seal for fluid flow in a reservoir (Fig. 12).
- (2) *Conduit*: site 2 displays low to average CD with few calcite veins. The rock matrix is not highly permeable, neither a hydraulic seal. However, because of its high fracture density and well-connected joints, the fault zone in site 2 is permeable to fluids (conduit). Site 4 has a high initial porosity (>10%) along with dense and well-connected fracture patterns, especially in the footwall (Fig. 6). On the other hand, the fault zone presents a continuous fringe of high CD values and a breccia core. But the CD fringe is thin (50 cm) and the core is fractured and not totally cemented. Consequently, site 4 is not a seal to fluid flow, but rather more likely a conduit.
- (3) *Mixed*: sites 3 and 5 exhibit thick and continuous high CD. In site 3, the duplex structure has high a CD, and in site 5, a megabreccia core cemented clasts in a clayey low-permeability matrix. So, at matrix scale, both sites form plurimetric thick and impermeable bands. The fault zone is also affected by numerous and highly connected fractures in the footwall, along with sparse and poorly connected fractures in the hanging wall. In subsurface reservoir conditions, sites 3 and 5 would have mixed hydraulic properties. They would be seals to fluid flow perpendicular to the fault plane but drain to flow parallel to the fault plane.

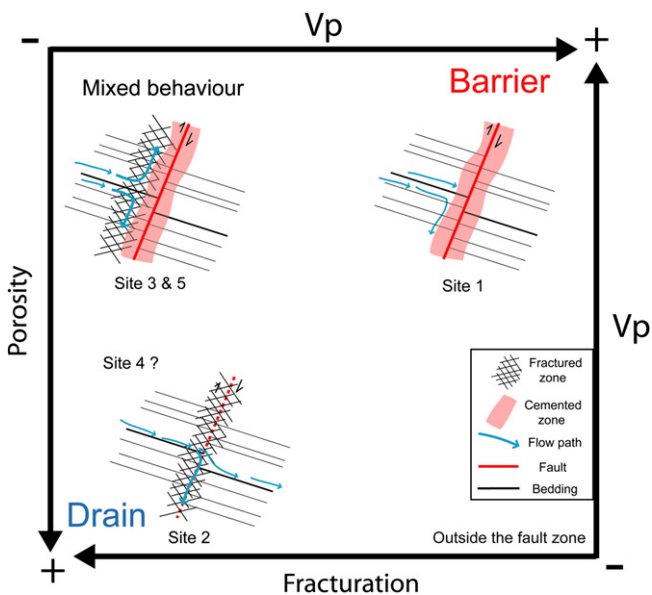


Fig. 12. Conceptual scheme of the three hydraulic types along the fault zone, depending on cementation and fracturation.

These three hydraulic classes (Fig. 12) are essentially consistent with the model proposed by Caine et al. (1996) for clastic rocks, which describe four fault-related classes: localized seal, localized conduit, distributed conduit, and combined conduit/seal. However, in the present study, the three hydraulic classes have been observed

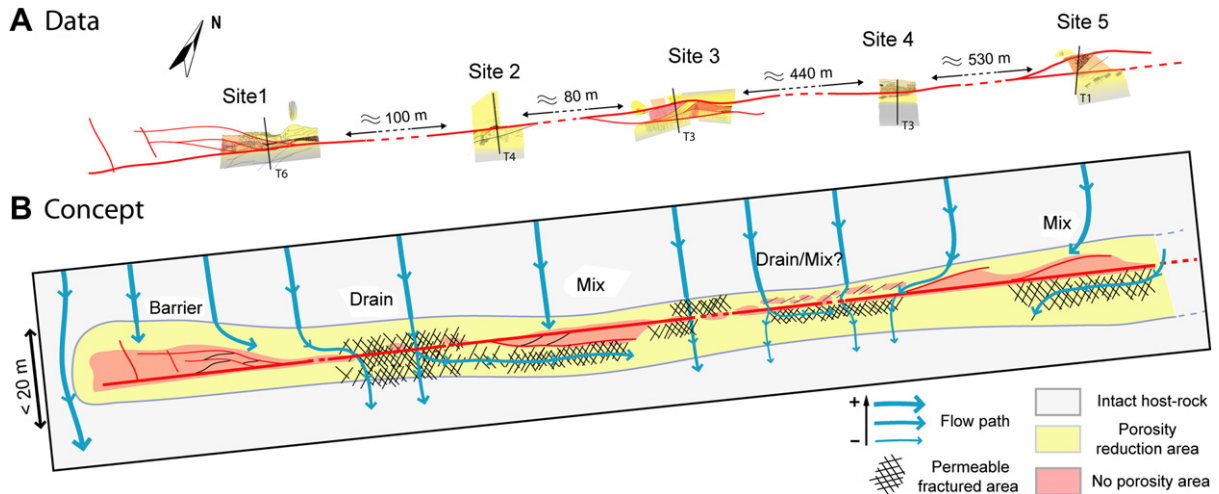


Fig. 13. Conceptual model of the fault hydraulic behavior lateral variations. A. Structural maps of the entire fault. B. Conceptual model.

along a single fault zone. This implies lateral variability in fault hydraulic properties (Fig. 13), and implicitly means that the fault cannot be considered as one single hydraulic object (e.g. Micarelli et al., 2006b). In subsurface reservoir conditions, the Castellás fault would be characterized as a heterogeneous seal/conduit/mixed hydraulic object (Fig. 13B).

5.4.1. Role of polyphase kinematics on fault diagenesis

The strain marker analysis conducted in the field as well as on samples and thin sections enabled reconstruction of the tectonic and diagenetic event chronology in the fault zone. In a first step, we set the Castellás fault as a normal fault, associated with calcite veins and the formation of gouge at site 1. Then, the fault was reactivated as a sinistral strike-slip structure, inducing the second breccia and stylolites observed on the five sites. Finally, open fractures crosscut all strain markers. This polyphased development of the fault resulted in a fault zone permeability evolution over time. For instance, the gouge at site 1 presents a laminated matrix and pendular calcite cement generally located under or at the clast contacts implying the presence of voids and fluid circulation in the fault core. As a consequence, the fault core acted as a conduit in the normal stage of the fault. Since the end of the Castellás fault activity, the fault core became tight ($\Phi = 0.3\%$) and was affected by many impermeable, calcite-filled tension gashes. In this way, the fault core became an impermeable seal. The numerous stylolites associated with the second breccia, especially at sites 1, 2 and 4, have likely led to CaCO_3 -rich fluids that enhanced the cementation within the fault zone (Tondi, 2007). We can conclude that the cementation of the Castellás fault zone is not an early or local process but occurred at several stages of fault reactivation over time. This is of significant importance for understanding the fault-sealing mechanism of the Castellás fault. In the gouge of site 1, the fault core sealing occurred early and resulted from sedimentary infilling materials (e.g. Gratier, 2011). At other sites of the study, the sealing is caused by the fluid-induced diagenetic cementation. By contrast, in silico-clastic rocks, the sealing commonly results from shale entrainment, smearing into the fault core (Fisher and Knipe, 2001; Eichhubl et al., 2009) or mechanical grain-size reduction (Billi et al., 2003). Labaume and Moretti (2001) have shown that initial host-rock porosity largely controls the deformation style in faulted sandstones. Fossen et al. (2007) pointed out that early deformation in deformation bands involves grain sliding, re organization or grain crushing, but requires a certain amount of porosity. In the host-rock carbonate grainstones of the Castellás fault, the grains are not deformed or

even re-organized. We can infer that the rock was porous but already stiff when the fault first occurred because of an early cementation diagenesis. It means that only grains only were porous, while the intergranular space was already filled/cemented, providing a stiff framework to the rock matrix, thus avoiding grains movements or grain-scales deformations.

6. Conclusions

In the present study, our results have led to an understanding of the present-day structure of the fault and to the development of a complex model linking the fault architecture and rock-physical properties, evolving over time. The model is relevant for fault zones with moderate throw in porous carbonates and can be compared with similar faults in subsurface carbonate reservoirs.

The high resolution structural and diagenetic maps have shown that the fault zone is a complex 3D volume of deformed rock displaying high frequency lateral variation. At each of the studied sites, the fault zones present peculiarities: The width of breccia core varies from 0 to 5 m; the fault zone has one or several slip planes; and the density and fracture pattern of the damage zone are different and asymmetric between footwall and hanging wall. These variable fault-zone styles are related to facies variations, to position along the fault, and to the fault throw. For instance, the relay zones and fault tips display the highest structural complexity.

The induced diagenesis in the fault zone revealed by the rock-physics properties affects a decameter-scale fringe on sides of the fault. In this fringe, physical properties strongly vary compared to the undamaged host rock. At the fault scale, the porosity decreases toward the fault plane, resulting in high P-wave velocity. At a lower scale, lateral variations in the porosity are linked to the heterogeneities of the fault zone architecture. The fault induced pressure-solution led to circulation of CaCO_3 -rich fluids, which likely participate to cementation of pores in the fault zone. Thus, the main sealing process of the Castellás fault is diagenetic (chemical) rather than mechanical; cementation enhanced fault stiffness and the fault's brittle behavior during fault reactivation. This phenomenon appears to be a particularity of carbonate fault zones with intra-granular matrix porosity.

The structural characterization of the fault coupled with rock-physics analyses lead to a reevaluation of past and present Castellás fault hydraulic properties. Each studied site along the fault presents different hydraulic characteristics (conduit, seal, or mixed). Therefore, this 1 km long fault in porous carbonate should

not be considered as a complete conduit or seal to fluid flow. On the contrary, it is formed by alternating conduit, seal, and mixed areas linked to the structural architecture of the fault. In 3D and in subsurface conditions, this implies complex multidirectional fluid flow along and through the fault.

This complex fault structure is important to consider in fluid flow simulations and predictions for fluid flow in reservoirs. A fault zone should be modeled as a heterogeneous 3D volume with key structural locations such as relays and tip extremities of the fault. Thus, in constructing numerical models of fault systems, a deterministic approach would seem to be more suitable than a probabilistic approach for capturing fault-zone properties (Childs et al., 1997).

Acknowledgments

The authors want to thank both anonymous reviewers for their valuable comments and corrections which led to considerable improvement of the present paper. We also thank the Sedimentary System and Reservoirs Lab staff especially, S. Souiki, A. Lavenu, P.-O. Bruna and A. Fournillon for their participation to the Fig. 6 (Suchard contest). P. Jeanne is acknowledged for his helpful contribution in sampling in the field, and P. Leonide for his advice in facies nomenclature. Finally, the authors wish to express their gratitude to Dan Hawkes from Lawrence Berkeley National Laboratory for his careful correction of English language quality.

Appendix A.

The high resolution structural mapping was carried out in five key sites along the fault (Fig. A1–A5). We analyzed these maps in terms of fault-zone width, internal architecture, heterogeneities, CD criterion, and fracture patterns.

A1. Site 1 structural and CD map description

The first site is the westernmost exposure of the Castellias fault and the largest studied outcrop. The structural and diagenetic map of site 1 relies on 10 transects crossing the fault exposure along 60 m. The main fault plane strikes N060 and dips 65°N (Fig. A1A); the width of the fault zone is ~15 m. In the hanging wall, the fault zone is composed of a mosaic of multiscale faults and fractures. We distinguish 13 anastomosed lenticular structural units (A to M in Fig. A1A) bounded by minor faults or decameter fractures. These faults and fractures are either parallel to the main fault plane or create an angle of more than 30° (Fig. A1C). Along the main fault plane, we observe a few-decimeters-thick (but discontinuous) fault core. It is composed of a gouge made of heterometric breccia with calcareous clasts and dark matrix (cf. Section 2.2). In the footwall, the fault-zone structure is simpler. Several minor normal faults with a centimetric throw can be distinguished, but no rock lenses are observed. The fracture pattern geometry is specific on each structural unit (Fig. A1A and C). For instance, no fractures affect the lens K, while the units I and J display a preferential fracture orientation. In Unit I, sub-vertical metric fractures are oriented N040–050° and turn in a direction parallel to the major fault plane, indicating a genetic relationship between fractures and the main fault. Conversely, in unit H, fractures are isotropic and decimetric in size. The structural units C, L and M are composed of cemented breccia, with clasts size ranging from a few centimeters to tens of centimeters.

The CD criterion varies as a function of the considered structural unit (Fig. A1A). Lenses J and F have a low CD criterion (0.7 and 0.5 respectively) induced by low cementation and no calcite veins. In contrast, the B, K, and M lenses have a high CD value (>2.5 in red on the map in Fig. A1A), owing to the entirely cemented fault rock and to numerous calcite veins. Structural units A, E, and I have

intermediate CD values (orange on the map). Note that according to the structural map, the structural units with the highest CD values are not systematically located close to the main fault plane.

At site 1, the coral rich layer (facies 2), is a marker level displaced by the main and minor faults. Dip measurements for the top of this sedimentary unit (Fig. A1A) show individual tilting and rotation in each of the lenses.

A2. Site 2

Site 2 is located 100 m east of site 1. The fault zone is more homogeneous than at site 1 (Fig. A2). Only one plane, striking N060 to N070 and dipping 65°N (in red on stereogram in Fig. A2C), shows evidence of slip with strike-slip sinistral slickensides (it is the main fault plane). We mapped 25 m of the fault and found the apparent width of the fault zone to be 10–15 m. In the footwall (south of the main fault plane), the fault zone is composed of three decametric fractures striking N040 to N060 (Fig. A2C), creating three individual structural units B, C, and F (Fig. A2A and B). Unlike in site 1, no dissimilar lenses are observed. In the hanging wall, an <1 m thick breccia body occurs close to the main fault plane (E on Fig. A2A), with badly delimited boundaries and striated blocks. North of the breccia body no decameter-scale fractures occur. The footwall block is intensely fractured. In the structural units B, C, and F (Fig. A2A), the rock is affected by two perpendicular and highly connected sets of joints, isolating decimetric blocks. One joint set is metric in length and fault-parallel, whereas the other set strikes N130 and is decimetric in size (Fig. A2C). In the structural unit D (Transect 2, Fig. 6), the rock is affected by fractures forming lenticular blocks parallel to the main fault plane (Fig. A2C). In the eastern part of the footwall, the rock is also fractured (but to a lower degree) by two sets striking N040 and N070 (Fig. A2A and C). In the hanging wall, fractures are rare, mostly horizontal, and poorly connected. Near the breccia lens (unit E), we observe sub-vertical metric fractures (e.g. N085 48°N), with their number increasing toward the main fault plane. In this unit, the CD criterion is the highest, reaching 3, owing to the breccia, the numerous calcite veins, and the tightly cemented clasts. Elsewhere, the CD criterion value is homogeneous and close to 1, constantly decreasing further away from the main fault plane (yellow to gray Fig. A2A).

To summarize, the fault zone in site 2 is drastically different from site 1. The structure is simpler, more homogeneous and quite symmetric, with only one main fault plane and with the CD value symmetrically toward the fault. Moreover, the fracture strikes are overall parallel to the main fault plane.

A3. Site 3

Site 3 is 80 m farther to the east of site 2. The structural and diagenetic map includes 50 m of the fault zone (Fig. A3A). Here, the fault zone is characterized by two major fault planes the northernmost one being the main fault plane, because it is laterally continuous over the entire studied area. Both fault-plane strikes vary from N059° to N070° from west to east (Fig. A3C), and bound a duplex structure comprising three sigmoid horses sensu Chinnery (1966) (B, C and D Fig. A3A and B). The fault dip remains unchanged along site 3, respectively sub-vertical for the main fault plane and about 50°N for the south fault plane. On the eastern part of the duplex, two narrow lenticular breccia zones lie along both fault planes. The first one (G Fig. A3A) is a fine calcareous breccia with an orange matrix; the second (F in Fig. A3A) contains a coarser-grained breccia showing less evidence of strain.

At site 3, the fracture pattern is asymmetric. South of the fault zone, the fractures are dense and highly connected, with two orthogonal joint sets (Fig. A3C). The first one is composed of metric

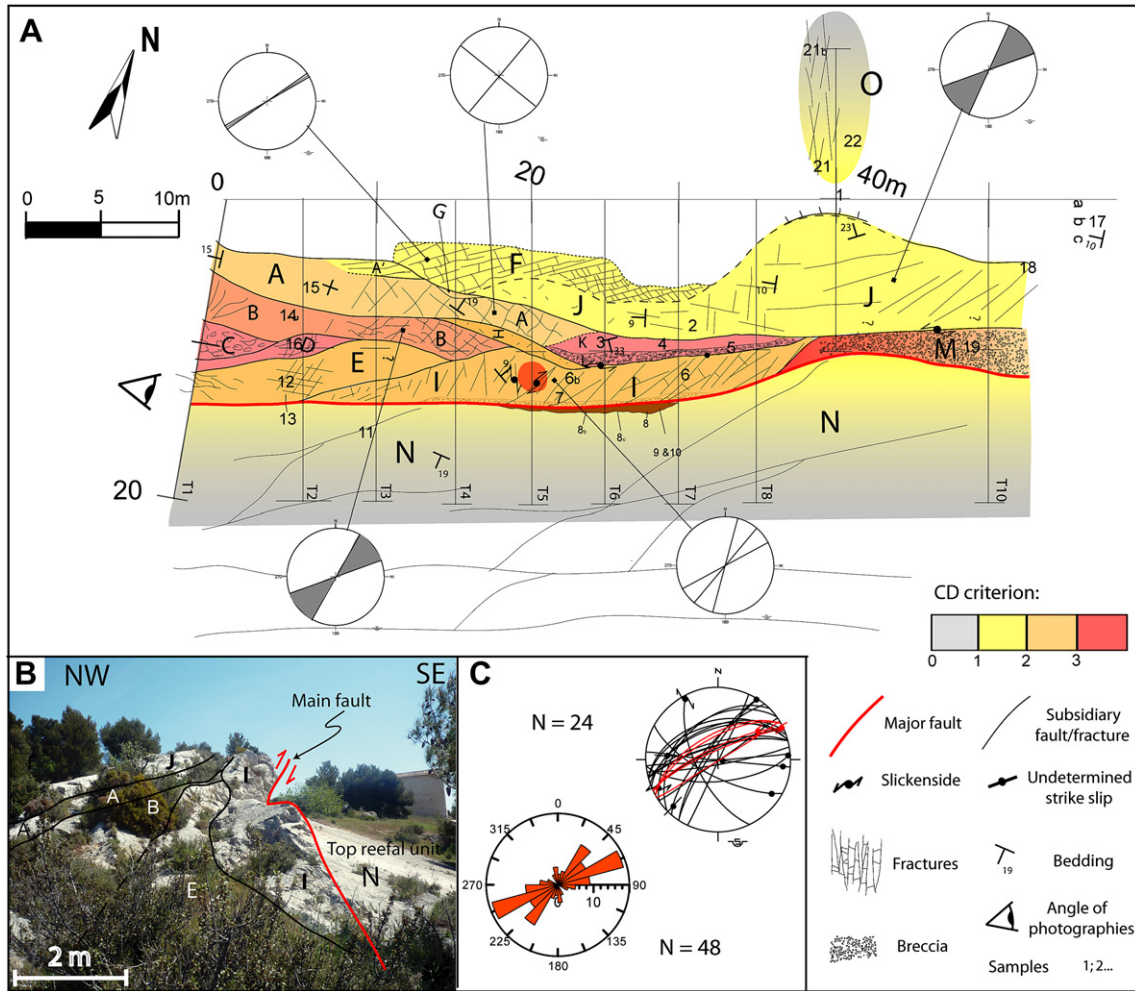


Fig. A1. A. Structural and CD map of the site 1 (gray area on schematic stereogram shows the strike dispersion of the joints). B. Site 1 photograph of the site 1 showing the main fault plane and lenticular structural units. C. Stereoplot of the main fault plane (red curves) and of plurimeter fractures/fault (black curves) (Lower hemisphere projection); rose diagram of fractures strike for the whole site.

fractures perpendicular to the southern fault, remaining orthogonal to the main fault plane even in the eastern part where the faults strike changes revealing a genetic link between the faults and the fractures. The second joint set is centimeter in size and disappears toward the fault, a few centimeters close to it. At the fault bend (transect 4 Fig. A3A), we find a local fracture set composed of lenticular and vertical fractures. North of the fault zone (unit A), fractures are scarce while west of the fault zone, we noticed a few unconnected decimeter-scale fractures, and a few areas of cemented breccia. In the duplex (B, C, and D in Fig. A3A) fractures striking N010 to N030 are poorly connected or unconnected. In the horse C, fractures are curved and branch parallel to the southern fault plane, and the horse termination is brecciated. The CD criterion is variable in the duplex but rather high. Horses' shapes B, C, and D have CD values higher than 2, resulting from the observed high cementation and calcite veins. On both sides of the two fault planes (units A and E), the CD values are lower 1.7 and 0.5, respectively. In the structural unit E, however, we find a 50 cm thick fringe with a higher CD value (CD = 2). This is correlated with the presence of many calcite veins, located close to the southern fault. The CD criterion rapidly decreases to 0 farther southward.

In brief, site 3 is distinguished by two principal fault planes delimiting a duplex structure, with high CD values. The fracture pattern is asymmetric between the northern and southern parts of the fault zone.

A4. Site 4

Site 4, located 440 m east of the third site, exhibits the narrowest fault zone with the simplest architecture of all the sites studied (Fig. A4A and B). It is composed of one fault plane striking N065; the fault zone is 10 m thick. No kinematic indicator has been noticed at this site. In the hanging wall, a 1–3 m thick continuous (at the map scale) breccia body has been observed. It is made of heterometric (mm to >cm) and smooth clasts (unit C on Fig. A4A). The breccia is affected by plurimeter scale fractures striking N025 to N035, and is bounded by several fault-parallel joints (Fig. A4C) and an isotropic joint set (unit A). In the footwall, the fractures are dense for the first 2 m adjacent to the fault. There, the rock is cut into decimetric, sublenticular blocks. Farther from the fault, in units E and B, joints are sparse or absent; the rock is undamaged and the bedding planes are clearly visible. The CD criterion shows fault-parallel variations. Despite the presence of many calcite veins in unit C, the breccia clasts are not totally crystallized, so the CD value is only 1.5. In the footwall, a meter-thick band with high CD (CD > 2) is observed near the fault; while CD values decrease rapidly (to 0) ~10 m from the main fault plane.

To sum up, the site 4 fault zone architecture is quite simple, with a breccia core and a slightly asymmetric fractured damaged zone on both fault sides.

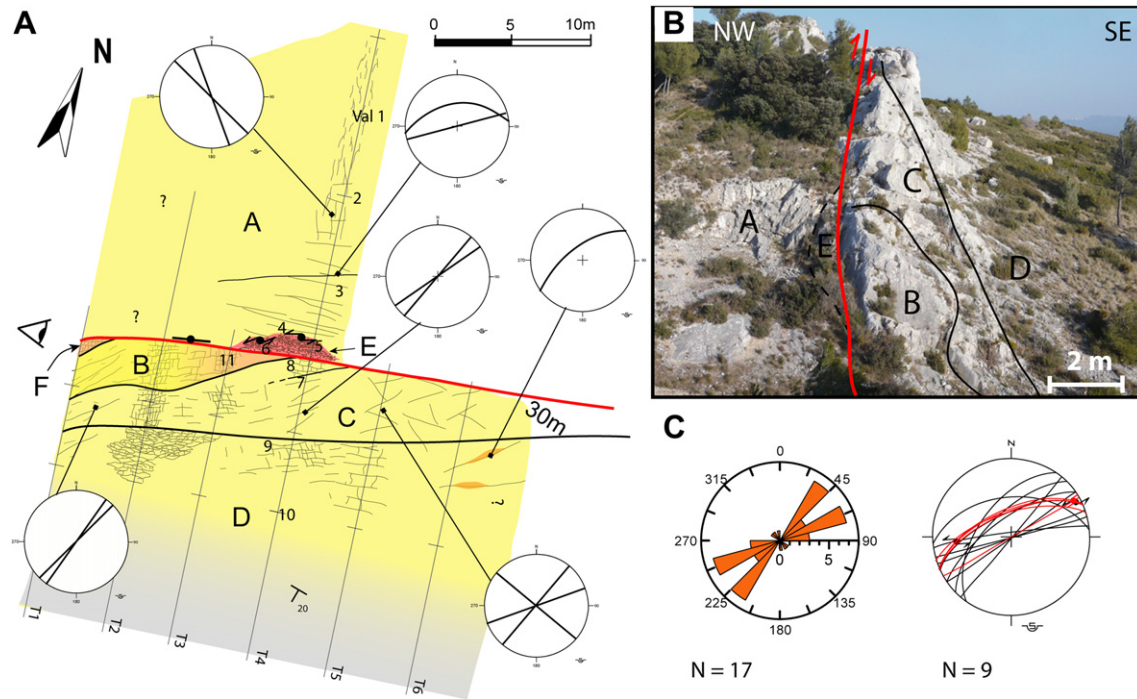


Fig. A2. A. Structural and CD map of the site 2. B. Photograph of the site 2 showing fault plane and structural units. C. Stereoplot of fault plane (red curves) and plurimeter fractures/fault (black curves) (Lower hemisphere projection); rose diagram of fractures strike.

A5. Site 5

At site 5, the fault zone is composed of two main fault planes striking N075–85°N (the southern plane the main fault plane in

Fig. A5A) and N062 35°N (northern plane in Fig. A5A). Subhorizontal striations (pitch = 14°W) are visible on the northern fault plane. Between both faults, two decametric fractures, respectively Fr1 striking N035 and Fr2 striking N045, form a wedge made of highly

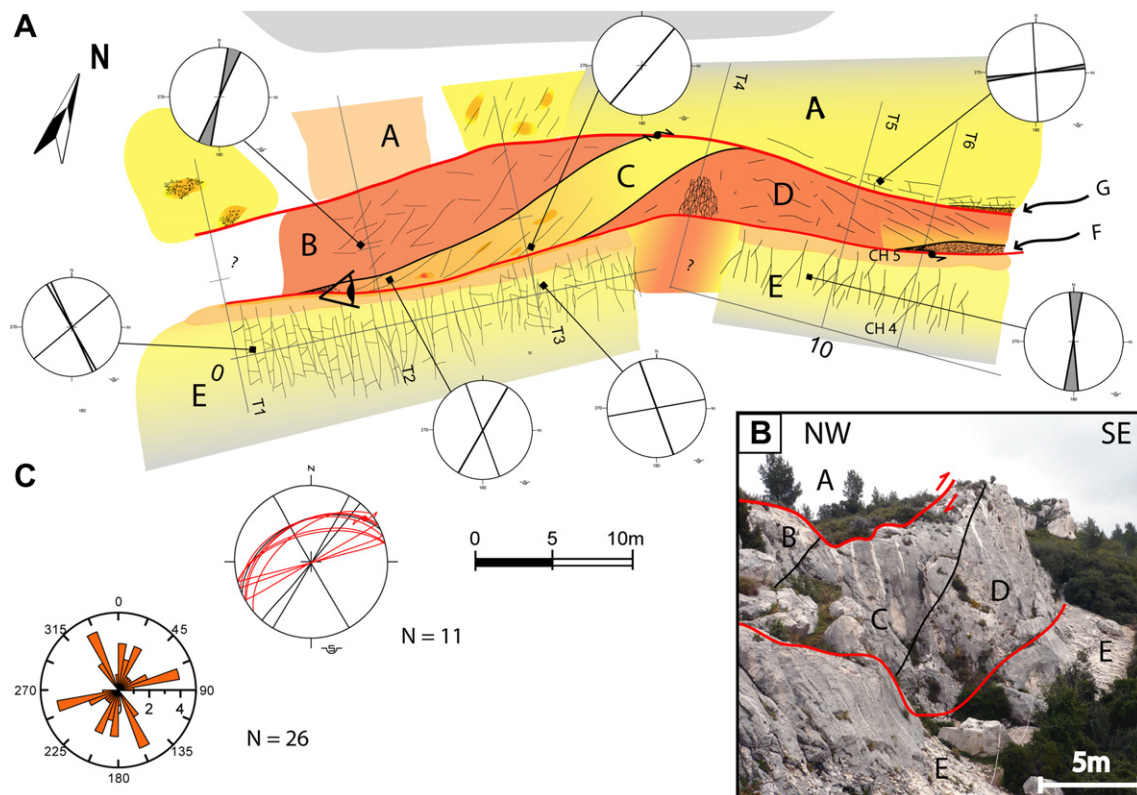


Fig. A3. A. Structural and CD map of the site 3. B. Photograph of the site 3 showing the two fault planes forming a duplex structure. C. Stereoplot of fault plane (red) and of plurimeter fractures/fault (Lower hemisphere projection); rose diagram of fractures strike.

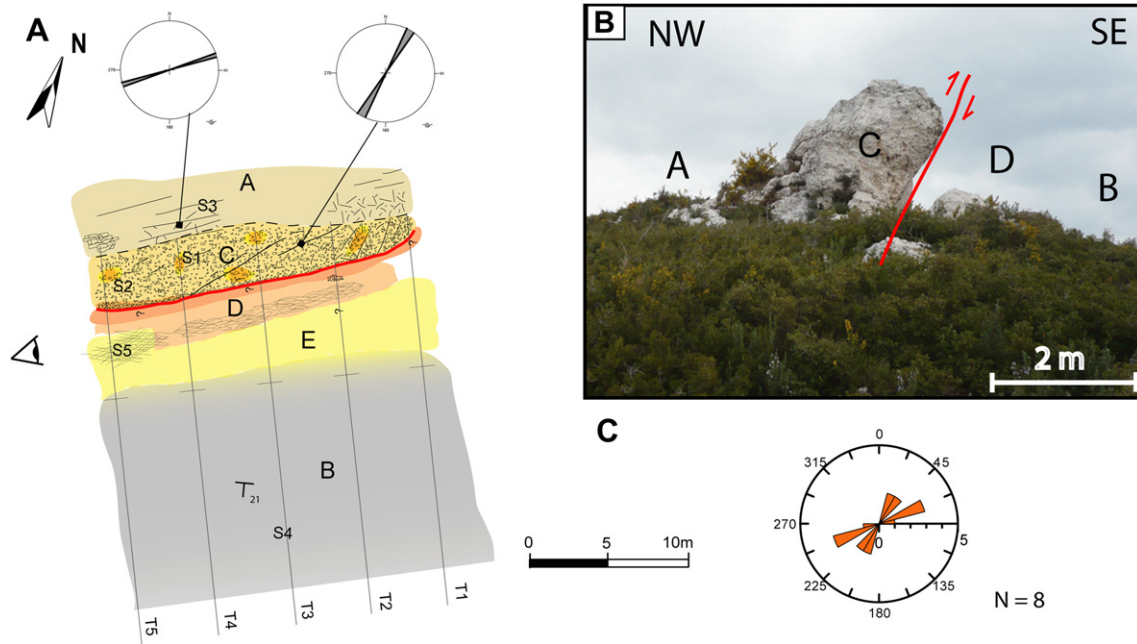


Fig. A4. A. Structural and CD map of the site 4. B. Photograph of the site 4 showing the fault plane and the breccia unit. C. Rose diagram of fractures strike.

deformed rocks including units B and F (Fig. A5A). Unit B is a heterometric megabreccia approximately 5 m thick, made of clasts ranging in size from 10 cm to plurimetric and of an argileous/silteous matrix. Clast sizes decrease toward the northern main fault. In the unit F, a second breccia fringe with rounded clasts of 5–20 cm exists near the southern fault plane. In the south part of the fault zone, the rock of unit G is highly fractured, with at least two perpendicular joint sets that cut the rock into decimetric cubic blocks close to the main fault. The main plurimeter joint set trends N080 (Fig. A5A and B). Ten meters apart from the fault, fractures are very sparse and

mainly horizontal. In the hanging wall (unit A & E), fractures are sparser than in the footwall and arranged in two sets parallel and perpendicular to the fault. The CD criterion is heterogeneous, particularly in unit B, where the breccia clasts are heterogeneously affected by strain and cementation, with CD varying from 2 to 3. Unit F shows a CD of 2. The overall CD values are rather symmetrical at site 5, decreasing on both sides of the fault zone.

In summary, the fault zone at site 5 is comparable to site 3 in that it is characterized by two fault planes. However, at site 5, a thick unit of breccia occurs between both faults.

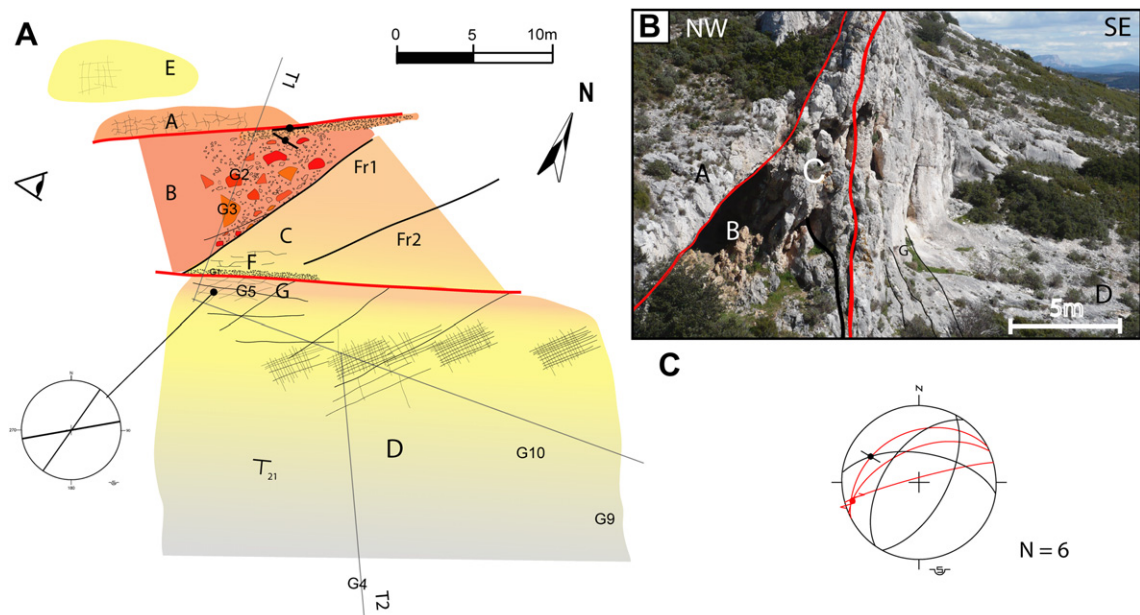


Fig. A5. A. Structural and CD map of the site 5. B. Photograph of the site 5 showing the two fault planes delimiting the megabreccia unit. C. Stereoplot of fault plane (red) and of plurimeter fractures (Lower hemisphere projection).

References

- Agosta, F., Alessandrini, M., Antonellini, M., Tondi, E., Giorgioni, M., 2010. From fractures to flow: a field-based quantitative analysis of an outcropping carbonate reservoir. *Tectonophysics* 490 (3–4), 197–213.
- Anselmetti, F.S., Eberli, G.P., 1993. Controls on sonic velocity in carbonates. *Pure and Applied Geophysics* 141, 287–323.
- Aydin, A., 2000. Fractures, faults, and hydrocarbon entrapment, migration and flow. *Marine and Petroleum Geology* 17 (7), 797–814.
- Bastesen, E., Braathen, A., 2010. Extensional faults in fine grained carbonates – analysis of fault core lithology and thickness-displacement relationships. *Journal of Structural Geology* 32 (11), 1609–1628.
- Baud, P., Vinciguerra, S., David, C., Cavallo, A., Walker, E., Reuschlé, T., 2009. Compaction and failure in high porosity carbonates: mechanical data and microstructural observations. *Pure and Applied Geophysics* 166, 869–898.
- Billi, A., Salvini, F., Storti, F., 2003. The damage zone-fault core transition in carbonate rocks: implications for fault growth, structure and permeability. *Journal of Structural Geology* 25 (11), 1779–1794.
- Blenkinsop, T.G., 2008. Relationships between faults, extension fractures and veins, and stress. *Journal of Structural Geology* 30, 622–632.
- Caine, J.S., Evans, J.P., Forster, C.B., 1996. Fault zone architecture and permeability structure. *Geology* 24 (11), 1025–1028.
- Chester, F.M., Logan, J.M., 1987. Composite planar fabric of gouge from the Punchbowl Fault, California. *Journal of Structural Geology* 9 (5–6), 621–634. IN5-IN6.
- Childs, C., Walsh, J.J., Watterson, J., 1997. Complexity in fault zone structure and implications for fault seal prediction. In: Møller-Pedersen, P., D.a. A.G. K.D. (Eds.), 1997. *Norwegian Petroleum Society Special Publications*, vol. 7. Elsevier, pp. 61–72.
- Chinnery, M.A., 1966. Secondary faulting: II. Geological aspects. *Canadian Journal of Earth Sciences* 3 (2), 175–190.
- Di Naccio, D., Boncio, P., Cirilli, S., Casaglia, F., Morettini, E., Lavecchia, G., Brozzetti, F., 2005. Role of mechanical stratigraphy on fracture development in carbonate reservoirs: insights from outcropping shallow water carbonates in the Umbria-Marche Apennines, Italy. *Journal of Volcanology and Geothermal Research* 148 (1–2), 98–115.
- Dunham, R.J., 1962. Classification of carbonate rocks according to depositional texture. *AAPG Memoir* 1, 108–121.
- Eberli, G.P., Baechle, G.T., Anselmetti, F.S., Incze, M.L., 2003. Factors controlling elastic properties in carbonate sediments and rocks. *The Leading Edge* 22 (7), 654–660.
- Eichhubl, P., Davatz, N.C., Becker, S.P., 2009. Structural and diagenetic control of fluid migration and cementation along the Moab fault, Utah. *AAPG Bulletin* 93 (5), 653–681.
- Faulkner, D.R., Jackson, C.A.L., Lunn, R.J., Schlische, R.W., Shipton, Z.K., Wibberley, C.A.J., Withjack, M.O., 2010. A review of recent developments concerning the structure, mechanics and fluid flow properties of fault zones. *Journal of Structural Geology* 32 (11), 1557–1575.
- Fisher, Q.J., Knipe, R.J., 2001. The permeability of faults within siliciclastic petroleum reservoirs of the North Sea and Norwegian Continental Shelf. *Marine and Petroleum Geology* 18 (10), 1063–1081.
- Fossen, H., Schultz, R.A., Shipton, Z.K., Mair, K., 2007. Deformation bands in sandstone: a review. *Journal of the Geological Society* 164, 755–769.
- Fournier, F., Borgomano, J., 2009. Critical porosity and elastic properties of microporous mixed carbonate-siliciclastic rocks. *Geophysics* 74 (2), E93–109.
- Fournier, F., Leonide, P., Biscarrat, K., Gallois, A., Borgomano, J., Foubert, A., 2011. Elastic properties of microporous cemented grainstones. *Geophysics* 76, E211–E226.
- Gattacceca, J., 2001. Cinématique du bassin liguro-provençal entre 30 et 12 Ma, implications géodynamiques. *Ecole des Mines de Paris*.
- Gaviglio, P., Vandycke, S., Schroeder, C., Coulon, M., Bergerat, F., Dubois, C., Pointeau, I., 1999. Matrix strains along normal fault planes in the Campanian White Chalk of Belgium: structural consequences. *Tectonophysics* 309, 41–56.
- Géraud, Y., Diraison, M., Orellana, N., 2006. Fault zone geometry of a mature active normal fault: a potential high permeability channel (Pirgaki fault, Corinth rift, Greece). *Tectonophysics* 426, 61–76.
- Gratier, J.P., 2011. Fault permeability and strength evolution related to fracturing and healing episodic processes (years to millennia): the role of pressure solution. *Oil & Gas Science and Technology – Revue d'IFP Energies Nouvelles*.
- Guyonnet-Benaize, C., Lamarche, J., Masse, J.-P., Villeneuve, M., Viseur, S., 2010. 3D structural modelling of small-deformations in poly-phase faults pattern. Application to the Mid-Cretaceous Durance uplift, Provence (SE France). *Journal of Geodynamics* 50 (2), 81–93.
- Jayet, O., 2009. Les faciès de fracturation dans les roches carbonatées: typologie, contrôles sédimentologiques et propriétés pétrophysiques (Crétacé inf. Bassin Sud Provençal). *University of Provence*, p. 63.
- Kim, Y.-S., Peacock, D.C.P., Sanderson, D.J., 2004. Fault damage zones. *Journal of Structural Geology* 26 (3), 503–517.
- Labaume, P., Moretti, I., 2001. Diagenesis-dependence of cataclastic thrust fault zone sealing in sandstones. Example from the Bolivian Sub-Andean Zone. *Journal of Structural Geology* 23 (11), 1659–1675.
- Lamarche, J., Borgomano, J., Caline, B., Gisque, F., Rigaud, S., Schroeder, S., Viseur, S., 2011. Characterization of fault-related dolomite bodies in carbonate reservoirs using Lidar scanner. In: Ole J. Martinsen, M.S., Andy Pulham, Peter Haughton (Eds.), 2011. *Outcrops Revitalized – Tools, Techniques and Applications*, SEPM Concepts in Sedimentology and Paleontology #10, pp. 175–194.
- Lamarche, J., Jayet, O., Lavenu, A., Gauthier, B., Guglielmi, Y., Demory, F., Masse, J.-P., Marié, L., 2010. *Mechanostratigraphy and Fracture Facies in Lower Cretaceous Carbonates of Provence*. European Geosciences Union General Assembly, Vienna.
- Lavenu, A.P.C., Lamarche, L., Gallois, A., Gauthier, B.D.M. Fracture patterns related to tectonics and diagenesis in naturally fractured carbonate reservoir analogue, La Nerthe anticline (southeastern France), in preparation.
- Leleu, S., 2005. Les cônes alluviaux Crétacé supérieur/Paléocène en Provence: traceurs de l'évolution morphotectonique des stades précoces de collision, PhD thesis. Louis Pasteur University.
- Lucia, F.J., 1999. *Carbonate Reservoir Characterization*, vol. XII. Springer, p. 226.
- Marchegiani, L., Van Dijk, J.P., Gillespie, P.A., Tondi, E., Cello, G., 2006. Scaling properties of the dimensional and spatial characteristics of fault and fracture systems in the Majella Mountain, central Italy. *Fractal Analysis for Natural Hazards* 261, 113–131.
- Martinez-Martinez, J., Benavente, D., del Cura, M.A.G., 2007. Petrographic quantification of brecciated rocks by image analysis. Application to the interpretation of elastic wave velocities. *Engineering Geology* 90 (1–2), 41–54.
- Masse, J.P., Philip, J., 1975. Paléogéographie et tectonique du Crétacé moyen en Provence: révision du concept d'Isthme Durancien. *Revue de Géographie Physique et de Géologie Dynamique* 18.
- Micarelli, L., Benedicto, A., Wibberley, C.A.J., 2006a. Structural evolution and permeability of normal fault zones in highly porous carbonate rocks. *Journal of Structural Geology* 28 (7), 1214–1227.
- Micarelli, L., Moretti, I., Jaubert, M., Moulouel, H., 2006b. Fracture analysis in the south-western Corinth rift (Greece) and implications on fault hydraulic behavior. *Tectonophysics* 426 (1–2), 31–59.
- Mitchell, T.M., Faulkner, D.R., 2009. The nature and origin of off-fault damage surrounding strike-slip fault zones with a wide range of displacements: a field study from the Atacama fault system, northern Chile. *Journal of Structural Geology* 31, 802–816.
- Moretti, I., 1998. The role of faults in hydrocarbon migration. *Petroleum Geoscience* 4 (1), 81–94.
- Morris, A.P., Ferrill, D.A., McGinnis, R.N., 2009. Mechanical stratigraphy and faulting in cretaceous carbonates. *AAPG Bulletin* 93 (11), 1459–1470.
- Peacock, D.C.P., 2002. Propagation, interaction and linkage in normal fault systems. *Earth-Science Reviews* 58 (1–2), 121–142.
- Rafavich, F., Kendall, C.H.S.C., Todd, T.P., 1984. The relationship between acoustic properties and the petrographic character of carbonate rocks. *Geophysics* 49 (10), 1622–1636.
- Robertson, E.C., 1983. Relationship of fault displacement to gouge and breccia thickness. *Mining Engineering* 35 (10), 1426–1432.
- Roche, V., 2008. Analyse structurale et géo-mécanique de réseau de failles du chaînon de La Fare les Oliviers (Provence). *Université de Montpellier 2*, p. 45.
- Sayers, C.M., 2008. The elastic properties of carbonates. *The Leading Edge* 27 (8), 1020–1024.
- Schroeder, C., Gaviglio, P., Bergerat, F., Vandycke, S., Coulon, M., 2006. Faults and matrix deformations in chalk: contribution of porosity and sonic wave velocity measurements. *Bulletin de la Société Géologique de France* 177 (4), 203–213.
- Shipton, Z.K., Cowie, P.A., 2003. A conceptual model for the origin of fault damage zone structures in high-porosity sandstone. *Journal of Structural Geology* 25 (3), 333–344.
- Steen, O., Andresen, A., 1999. Effects of lithology on geometry and scaling of small faults in Triassic sandstones, East Greenland. *Journal of Structural Geology* 21 (10), 1351–1368.
- Surma, F., Geraud, Y., Pourcelot, L., Gauthier-Lafaye, F., Clavaud, J.B., Zamora, M., Lespinasse, M., Cathelineau, M., 2003. Porosity microstructures of a sandstone affected by a normal fault. *Bulletin de la Société Géologique de France* 174 (3), 295–303.
- Tiabi, D., Donaldson, E.C., 1996. *Petrophysics: Theory and Practice of Measuring Reservoir Rock and Fluid Transport Properties*, vol. XIV. Gulf Professional Publishing, p. 706.
- Tondi, E., Antonellini, M., Aydin, A., Marchegiani, L., Cello, G., 2006. The role of deformation bands, stylolites and sheared stylolites in fault development in carbonate grainstones of Majella Mountain, Italy. *Journal of Structural Geology* 28, 376–391.
- Tondi, E., 2007. Nucleation, development and petrophysical properties of faults in carbonate grainstones: evidence from the San Vito Lo Capo peninsula (Sicily, Italy). *Journal of Structural Geology* 29 (4), 614–628.
- Twiss, R.J., Moores, E.M., 1992. In: *Freeman (Ed.), Structural Geology*, p. 532.
- Vanorio, T., Mavko, G., 2011. Laboratory measurements of the acoustic and transport properties of carbonate rocks and their link with the amount of microcrystalline matrix. *Geophysics* 76, E105–E115.
- Wibberley, C.A.J., Shimamoto, T., 2003. Internal structure and permeability of major strike-slip fault zones: the Median Tectonic Line in Mie Prefecture, Southwest Japan. *Journal of Structural Geology* 25 (1), 59–78.
- Wibberley, C.A.J., Yielding, G., Di Toro, G., 2008. Recent advances in the understanding of fault zone internal structure: a review. In: *Geological Society, London, Special Publications*, vol. 299(1), pp. 5–33.